UC Santa Barbara
UC Santa Barbara Previously Published Works

Title

Quantification of three-dimensional folding using fluvial terraces: A case study from the Mushi anticline, northern margin of the Chinese Pamir

Permalink

Authors

Li, Tao
Chen, Jie
Thompson, Jessica A
et al.

Peer reviewed

Quantification of three-dimensional folding using fluvial terraces: A case study from the Mushi anticline, northern margin of the Chinese Pamir

Tao Li,[1] Jie Chen,[1] Jessica A. Thompson,[2] Douglas W. Burbank,[2] and Xiaodong Yang [1]

[1] Fold deformation in three dimensions involves shortening, uplift, and lateral growth. Fluvial terraces represent strain markers that have been widely applied to constrain a fold's shortening and uplift. For the lateral growth, however, the utility of fluvial terraces has been commonly ignored. Situated along northern margin of Chinese Pamir, the Mushi anticline preserves, along its northern flank, flights of passively deformed fluvial terraces that can be used to constrain three-dimensional folding history, especially lateral growth. The Mushi anticline is a geometrically simple fault-tip fold with a total shortening of 740 ± 110 m and rock uplift of ~1300 m. Geologic and geomorphic mapping and dGPS surveys reveal that terrace surfaces perpendicular to the fold's strike display increased rotation with age, implying the fold grows by progressive limb rotation. We use a pure-shear fault-tip fold model to estimate a uniform shortening rate of $1.5 + 1.3/-0.5$ mm/a and a rock-uplift rate of $2.3 + 2.1/-0.8$ mm/a. Parallel to the fold's strike, longitudinal profiles of terrace surfaces also display age-dependent increases in slopes. We present a new model to distinguish lateral growth mechanisms (lateral lengthening and/or rotation above a fixed tip). This model indicates that eastward lengthening of the Mushi anticline ceased by at least ~134 ka and its lateral growth has been dominated by rotation. Our study confirms that terrace deformation along a fold's strike not only can constrain the lateral lengthening rate but can serve to quantify the magnitude and rate of lateral rotation: attributes that are commonly difficult to define when relying on other geomorphic criteria.

1. Introduction

[2] Fold deformation in three dimensions involves shortening, uplift, and lateral growth (Figure 1). As amplitude and length increase due to folding, interactions with erosion and deposition create a fold's morphology and its superimposed drainage pattern. The two-dimensional, transport-parallel fold architecture (due to shortening and uplift), which is a typical focus of most studies and related fold theory, can be retrieved based on a combination of pregrowth strata with time-controlled growth strata and geomorphic markers, e.g., *Suppe et al.* [1992], *Storti and Poblet* [1997], *Simoes et al.* [2007], and *Goode and Burbank* [2011]. Lateral growth, the integrated aspect of fold deformation, is commonly defined by two end-member mechanisms: outward migration of fold tips (lateral lengthening) or differential uplift and upward rotation of the fold surface above a fixed tip without lengthening (lateral rotation) [*Jackson et al.*, 1996; *Mueller and Talling*, 1997; *Delcaillau et al.*, 1998; *Keller et al.*, 1998, 1999; *Burbank et al.*, 1999; *Manighetti et al.*, 2001; *Bennett et al.*, 2005, 2006; *Chen et al.*, 2007; *Schlagenhauf et al.*, 2008; *Burbank and Anderson*, 2011]. Lateral lengthening can be one of the most rapid surface-deformation processes, and geomorphic criteria, such as drainage density and both water and wind gaps, as well as characteristic drainage patterns, are commonly used to estimate lengthening directions and rates [*Jackson et al.*, 1996; *Delcaillau et al.*, 1998; *Keller et al.*, 1998, 1999]. In contrast, far fewer studies of lateral rotation as deduced from geomorphic criteria have been conducted, e.g., *Manighetti et al.* [2001] and *Schlagenhauf et al.* [2008].

[3] As a useful geomorphic strain marker linking underlying structure to surface deformation, approximately isochronous fluvial terraces have been successfully used to deconvolve shortening and uplift of a fold. For example, *Rockwell et al.* [1988] used fluvial terraces to constrain shortening and uplift rates of flexural slip folds in south California; *Lavé and Avouac* [2000] and *Thompson et al.* [2002] estimated the shortening rates of fault-bend folds in the Himalaya foreland

[1]State Key Laboratory of Earthquake Dynamics, Institute of Geology, China Earthquake Administration, Beijing, China.

[2]Department of Earth Science, University of California, Santa Barbara, California, USA.

Corresponding author: J. Chen, State Key Laboratory of Earthquake Dynamics, Institute of Geology, China Earthquake Administration, Huayanli 1#, Beitucheng West Street, Beijing, 100029, China. (chenjie@ies.ac.cn)
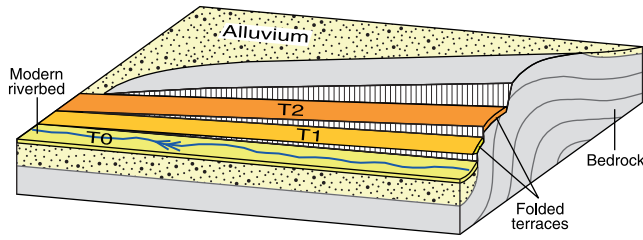
Figure 1. Sketch showing deformation of fluvial terraces in response to three-dimensional folding. Note that terrace surfaces are not only folded in cross section perpendicular to the fold's strike, but when compared with the modern riverbed, they also tilt in a longitudinal direction parallel with the fold's strike.

and the Kyrgyzstan Tian Shan, respectively; *Scharer et al.* [2006] and *Simoes et al.* [2007] investigated the methods using deformed terrace surfaces to constrain structural styles, shortening, and uplift of detachment folds in the southern Tian Shan and pure-shear fault-tip folds in Taiwan, respectively. Syntectonic, passively deformed terraces, however, also can reflect lateral growth (Figure 1): a phenomenon that has been much less thoroughly investigated. Along northern margin of Chinese Pamir (Figure 2a), the Mushi anticline is a geometrically simple fold. Erosion by a nearby river and extensive deposition of alluvium on the flanks of the fold obscure any growth strata that might allow us to reconstruct deformation during folding. Fortunately, flights of wide, continuous, and clearly deformed fluvial terraces are preserved over most of the northern half of the fold and span the fold axis (Figure 3b). These terraces provide a rare chance to exploit their deformed geometry to develop a three-dimensional folding history. We conducted detailed geologic and geomorphic mapping, along with high-precision dGPS surveys and optically stimulated luminescence dating of terraces, to quantify the shortening, uplift rates, and changes in the folding style through time, as well as the initiation age of the fold. In addition, a new kinematic model is developed to explore the use of
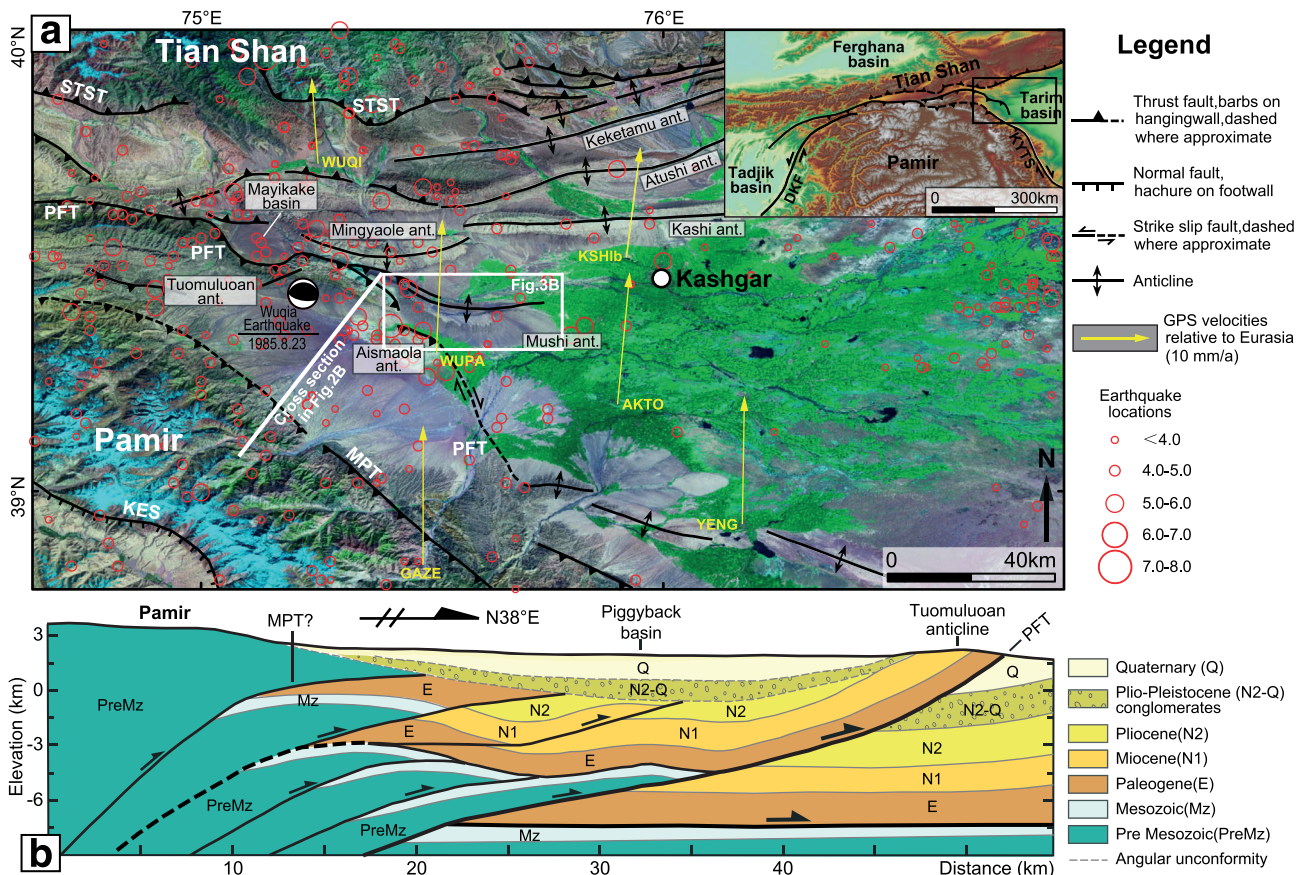
Figure 2. (a) Advanced Spaceborne Thermal Emission and Reflection Radiometer (ASTER) satellite image of northern margin of Chinese Pamir and the southern Tian Shan. Inset shows the simplified tectonic setting and topography of the study area. DKF: Darvaz-Karakul Fault, KYTS: Kashgar-Yecheng Transfer System, MPT: Main Pamir Thrust, PFT: Pamir Frontal Thrust, STST: South Tian Shan Thrust. Site abbreviations and GPS velocities (yellow arrows) are relative to stable Eurasia from *Zubovich et al.* [2010] and shows a ~7–9 mm/a convergent rate across the zone of the Pamir Frontal Thrust. Earthquake locations are from the U.S. Geological Survey (USGS) seismic catalog for the period 1973–2010. (b) Interpreted seismic profile between the Main Pamir Thrust and Pamir Frontal Thrust from *Chen et al.* [2010]. The base of N2-Q Formation in the piggyback basin is an angular unconformity, but it is, in addition, a main erosion surface (erosional unconformity) since it clearly truncates the thrust units. The section location is marked in Figure 2a. Modified from *Li et al.* [2012].
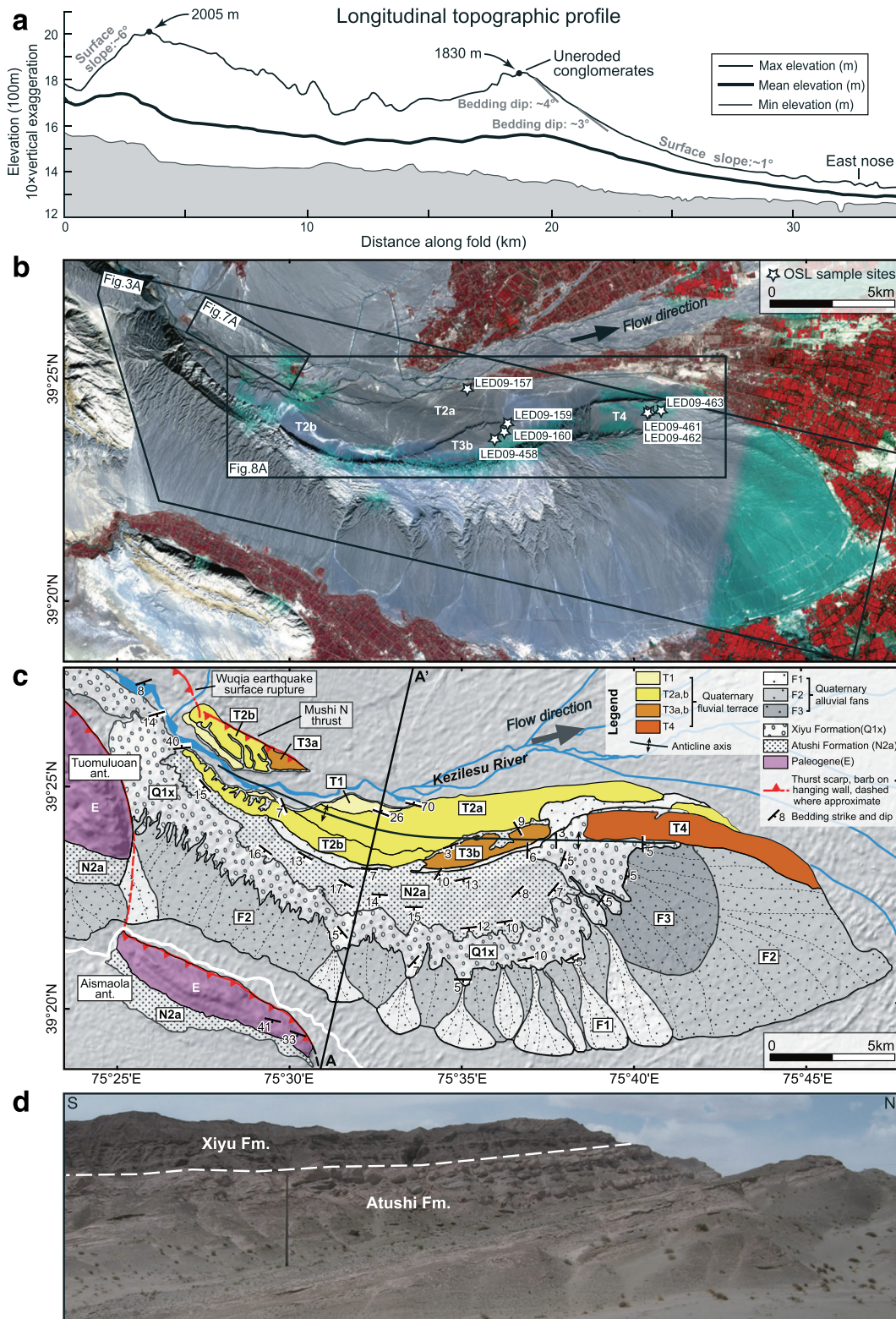
Figure 3. (a) An 8 km wide topographic swath profile along the crest of the Mushi anticline displaying a gentle eastward taper in the fold's lateral growth direction. For swath location, see Figure 3b. Topography is from the 30 m ASTER Global Digital Elevation Model (GDEM). The Xiyu conglomerate defines two local elevation maxima. Note that the dip of the underlying bedrock is subparallel to the fold surface near the eastern topographic peak. (b) ASTER satellite image and OSL sample locations of the Mushi anticline. The image area is outlined in Figure 2b. (c) Geologic map of the Mushi anticline based on Kang et al. (unpublished manuscript, 1978) and our additional field mapping. (d) Photograph of the contact between the Xiyu Formation and the Atushi Formation on the southern limb of the Mushi anticline.

terrace deformation along a fold's strike to define lateral fold growth mechanisms (lateral lengthening, rotation, or a combination of both) and associated deformation rates. Application of this model to the Mushi anticline indicates that eastward lengthening of the fold ceased by at least ~134 ka and that lateral rotation of the fold tip has dominated since then.

2. Tectonic Setting

[4] The Pamir lies in the northwestern region of the Indo-Asian collision zone. The northern Pamir has indented northward ~300 km [*Burtman and Molnar*, 1993] since mid-Cenozoic times (25–20 Ma) [*Sobel and Dumitru*, 1997]. This indentation was accommodated by south-dipping intra-continental subduction along the Main Pamir Thrust and was coupled with sinistral strike-slip on the Darvaz-Karakul Fault on its western margin and dextral strike-slip of the Kashgar-Yecheng Transfer System on its eastern margin (Figure 2a inset) [*Burtman and Molnar*, 1993; *Bazhenov et al.*, 1994; *Negredo et al.*, 2007; *Cowgill*, 2010]. In response to the indentation, structures along the southern margin of the Tian Shan were reactivated at 25–18 Ma [*Yin et al.*, 1998; *Sobel et al.*, 2006] and deformation then episodically migrated southward to produce a series of subparallel fold belts (Figure 2a) [*Chen et al.*, 2002, 2007; *Scharer et al.*, 2004, 2006; *Heermance et al.*, 2008]. The Kashi-Atushi fold system, as the youngest fold belt formed in the forelandward migration of the Tian Shan, accommodates an average Quaternary shortening rate of ~5 mm/a [*Chen et al.*, 2002; *Scharer et al.*, 2004].

[5] Situated between the Pamir and the southern Tian Shan, the western Tarim basin subsided significantly due to loading by these two ranges and was filled by an 8 to 12 km thick, upward-coarsening clastic sedimentary wedge. Based on interpretation of seismic profiles and analysis of drill hole data and regional lithology, *Xiao et al.* [2000] suggested that two regional detachment surfaces commonly occur across the western Tarim. The deeper one, at approximately 13 km depth, comprises Cambrian dolomite, limestone, gypsum, and gypsiferous mudstone. The shallower detachment, between 7 and 10 km depth, is composed of Paleogene gypsum, gypsiferous mudstone, and limestone. Existence of two detachment surfaces facilitates forelandward propagation of the Pamir and the Southern Tian Shan. Although whether a detachment surface links the Pamir with the southern Tian Shan is still debated, seismic data suggest that such linkage is likely. Hence, attributing deformation near their apparent interface to one orogen or the other can be somewhat arbitrary.

[6] Since Late Miocene-Pliocene, activity along the Kashgar-Yecheng Transfer System ceased [*Cowgill*, 2010; *Sobel et al.*, 2011], and the Pamir joined together with the Tarim basin to collide with the Tian Shan. This regional tectonic transformation may have caused the deformation front to transfer from the Kashgar-Yecheng Transfer System and its northwestern extension (the Main Pamir Thrust: the boundary fault between the Pamir and the Tarim basin) to the Pamir Frontal Thrust, an interference zone along the interface of the Pamir and the Tian Shan. The Pamir Frontal Thrust is a zone of active thrust faulting and folding that was activated in the latest forelandward propagation sequence of the Pamir along a detachment surface localized within Paleogene gypsum (Figure 2b). The Pamir Frontal Thrust can be subdivided into several segments, each displaying different deformation patterns and retaining relatively independent evolving histories [*Chen et al.*, 1997]. A ~7–9 mm/a convergent rate from GPS data [*Zubovich et al.*, 2010] and frequent earthquakes, including the 1985 Wuqia M7.4 event (Figure 2a) [*Feng*, 1994], reflect ongoing and concentrated activity on the fault. Adjacent to the Mayikake basin, the Pamir Frontal Thrust has accommodated a uniform shortening rate of ~5–7 mm/a since at least ~0.35 Ma [*Li et al.*, 2012].

3. Geology, Geomorphology, and Balanced Cross Section of the Mushi Anticline

3.1. Stratigraphy, Structure, and Geomorphology

[7] Located to the south of the Kashi-Atushi fold system, the Mushi anticline extends eastward from the eastern end of the Tuomuluoan anticline, which grew above one segment of the south-dipping Pamir Frontal Thrust, to where the nose plunges into the depositional plain of the western Tarim basin (Figure 2a). On the surface, the fold exhibits an ESE-trending topographic relief that is ~32 km long by 4 to 10 km wide (Figure 3b). Most of the northern half of the fold is characterized by wide, flat fluvial terraces of the Kezilesu River, whereas its southern and eastern flanks are covered by three stages of alluvial fans (Figure 3c).

[8] The anticline exposes two moderately lithified sedimentary sequences (Figure 3c): the Pliocene Atushi Formation and the Pleistocene Xiyu Formation. The Atushi Formation comprises fluvial-lacustrine deposits and is primarily well-bedded, gray-yellow, brownish, and gray-green sandstone and mudstone, whereas stratigraphically higher levels include pebble conglomerate layers. Exposure of the Atushi Formation is concentrated in the core of the fold where it displays a total outcrop thickness of 700–900 m (Kang et al., Structure features and an assessment of hydrocarbon potential of the Kashi depression of the Tarim basin, Xinjiang, unpublished manuscript, 1978, hereinafter referred to as Kang et al., unpublished manuscript, 1978). Conformably above the Atushi Formation (Figures 3c and 3d), the Xiyu Formation is a suite of massive, thickly bedded, pebble-to-cobble conglomerate, typical of deposits of alluvial fans and gravel-bedded braided rivers. Paleomagnetic studies from the Kashi-Atushi fold system show that the Xiyu Formation is clearly time-transgressive with its base ranging from ~16 Ma in the north to <1 Ma in the south [*Chen et al.*, 2002, 2007; *Heermance et al.*, 2007; *Charreau et al.*, 2009]. With a total thickness of ~500 m, the Xiyu Formation is exposed mainly in the southern limb and both noses of the Mushi fold. The conformable contact between the Atushi and Xiyu Formations indicates that the Mushi anticline initiated later than the lower boundary age of the Xiyu Formation, which is ~1.6 Ma based on magnetostratigraphy on the southern limb of the Mingyaole anticline that is found nearby (Figure 2a) [*Chen et al.*, 2005]. A cosmogenic burial age of ~1.8 Ma (J. Thompson et al., manuscript in preparation, 2013) also suggests fold initiation in early to middle Pleistocene.

[9] The Mushi anticline is an asymmetric, overall north-vergent fold with a steep northern limb (40°–70°) and a gentle southern limb (5°–18°) (Figure 3c). Along strike of the fold, the western end exhibits steeper beds and tighter folding than the eastern end. Along the northwestern part of the anticline, a ~5 km long ESE-trending thrust zone
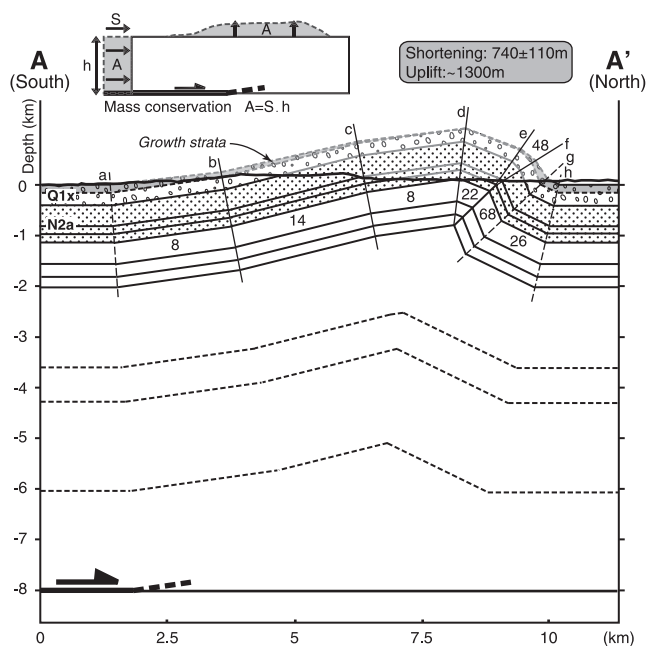
Figure 4. Geological cross section of the Mushi anticline (for location, see Figure 3c). The depth to the detachment surface is determined from seismic reflection profiles across neighboring areas [*Chen et al.*, 2002, 2007; *Chen et al.*, 2010; *Scharer et al.*, 2004]; the width is constrained by surface exposures and the outer limb of folding expressed in satellite image. Deeper horizons are dashed because the actual deformation style at these levels is speculative. The top gray shaded area enveloped by dashed lines represents growth strata: its upper and lower boundaries are speculative. Above the modern topography, the bedding lines are lighter gray. The Mushi fold can be subdivided into a few dip domains bounded by hinges a–h, which also appear on topographic profiles in Figures 7, 8, and 9. The excess area method (inset at the top) [*Epard and Groshong*, 1993] gives a total shortening of 740 ± 110 m and uplift of ~1300 m.

produces several subparallel fault scarps on the surface (Figure 3c). Farther west, these fault scarps terminate close to the eastern end of the 1985 Wuqia earthquake surface rupture [*Feng*, 1994; *Chen et al.*, 1997].

[10] The Mushi anticline also exhibits a strong longitudinal asymmetry. Although the fold is doubly plunging, the structural crest is located ~5 km (~15% of the length of the fold) from the western tip (Kang et al., unpublished manuscript, 1978), instead of lying halfway along the distance of the fold. Furthermore, according to longitudinal topographic section of the anticline from its western end (Figure 3a), the highest topography along the fold rises rapidly eastward to a peak, maintains low relief through the fold's center before increasing to another peak, and finally decreasing gradually to the east. Whereas the western geomorphic termination of the fold forms a blunt, steeply plunging, broad fold nose, the eastern termination is an elongated, gently plunging arc whose axis dips at <1.0° across the last 9 km of the topographically expressed fold nose. The two topographic peaks are coincident with outcrops of the Xiyu conglomerate, which is considerably more erosion-resistant than the Atushi sandstone and siltstone; the latter being coincident with low relief in

the middle of the fold. Therefore, the erodability contrast of the bedrock exerts a fundamental control on the mesoscale topography of the Mushi fold. Once the carapace of conglomerate is breached, erosion accelerates and attacks the weak strata in the core of the fold.

[11] According to geomorphic criteria related to lateral growth of a fold [*Keller et al.*, 1999], the geomorphic attributes of the Mushi anticline imply a primarily growth from west to east. Evidence for this eastward growth includes: (i) the anticline is more tightly folded at western part than the eastern part, and the structural crest is located ~5 km (15%) from the western tip; (ii) the western fold nose is blunt, steeply plunging, and broad, whereas the eastern termination is elongate and gently plunging, suggesting the lateral growth toward the east; (iii) although there are two topographic peaks, the terrain and the differences among elevation maxima, average, and minima along the strike of the anticline still display a roughly gradual decrease from west to east; (iv) the more deeply incised gullies, the smaller scale alluvial fans and shorter individual channels indicating deeper incision and higher drainage network density at the western part; and (v) the orientation of drainages on the fold rotates from nearly N-S on its western part to W-E at its eastern end. The asymmetric, primarily eastward growth of the Mushi anticline may be attributable to the nearby, strongly deformed Tuomuluoan anticline, which inhibits the Mushi anticline's westward growth. In contrast, the broad, undeformed span of the Tarim Basin permits unimpeded propagation of the fold's eastern tip.

[12] The Mushi's spatial continuation to its west with the Tuomuluoan anticline (Figure 2a), its north-vergent asymmetric geometry, and its lateral propagation to the east make it a reasonable inference that the Mushi fold is developing above a splay of the north-vergent Pamir Frontal Thrust. As such, we consider Mushi as part of the Pamir orogeny.

3.2. Balanced Cross Section

[13] Because seismic reflection profiles were not available across the Mushi anticline, we try to constrain its subsurface geometry and construct a balanced cross section by combining mapping data of Kang et al. (unpublished manuscript, 1978), additional field observations and structural measurements, and seismic reflection data from areas within ~25 km of the fold. One important feature observed in seismic reflection profiles across the Kashi-Atushi fold system and the piggyback basin between the Pamir Frontal Thrust and the Main Pamir Thrust is an essentially flat-lying, strong reflector at ~9 km depth below the land surface (Figure 2b), which we identify as a regional detachment surface mainly composed of Paleogene gypsum [*Chen et al.*, 2002, 2007; *Scharer et al.*, 2004; *Chen et al.*, 2010]. Beneath the Kashi anticline to the north of the Mushi fold, the reflector is shallower: ~7 km below land surface [*Chen et al.*, 2007]. Because we interpret these detachments to be linked, we suggest a detachment depth for the Mushi anticline of 8 ± 1 km (Figure 4). Assuming that undeformed strata from both sides of the fold had the same prefolding elevations and that the thicknesses of the Atushi Formation and the Xiyu Formation remained constant during folding, we created a balanced cross section of the Mushi anticline (A-A': Figure 4) in which the anticline is interpreted as a thrust-tip fold controlled by a detachment surface or a blind ramp. Although some thrusting occurs in the northwestern area
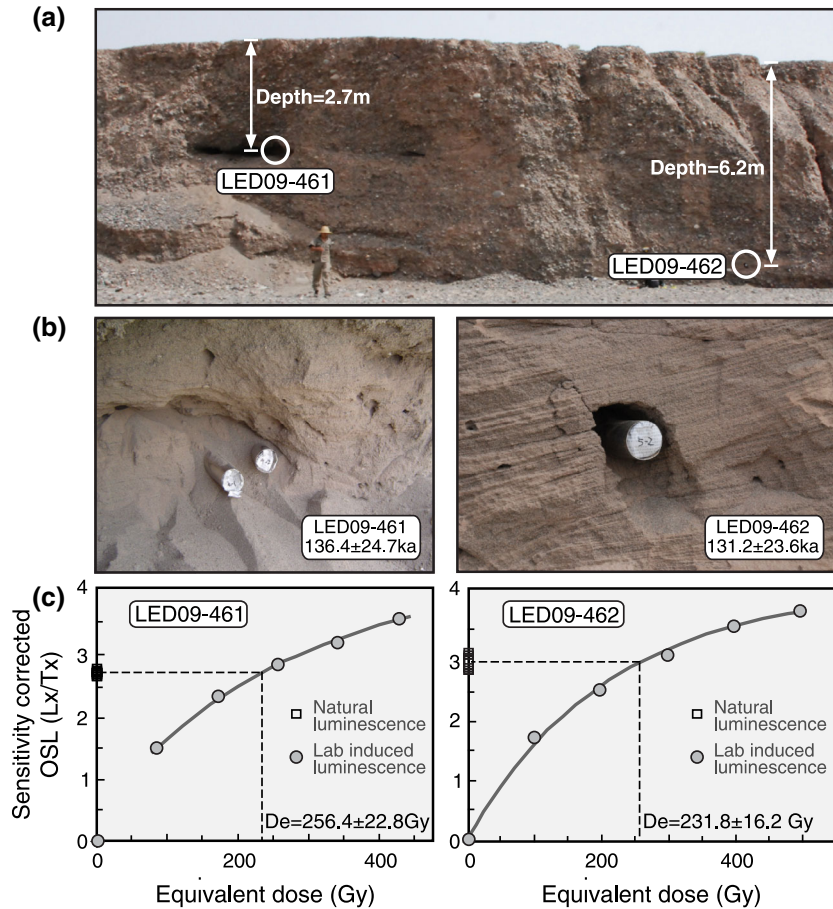
Figure 5. Photographs of (a) sampling locality and (b) interbedded silt and fine sand, and (c) growth curves and equivalent doses (De) for samples LED09-461 and LED09-462 within the T4 terrace deposits.

of the fold, it is not interpreted as the main fault producing the anticline, because it lacks significant lateral continuity. More importantly, a fold width of ~8 km near this thrust and a detachment depth of ~8 km suggest that the ramp (if it exists) producing the fold should dip ~45°, which is much steeper than any observed bedding dips (5°–18°) along the southern fold limb (Figure 3c). Hence, the thrust in the northwestern area is likely to be a secondary fault that formed during folding.

[14] The cross section depicts a clearly asymmetric geometry of the Mushi fold whose northward vergence is similar to that of the asymmetric Kashi and Mingyaole folds in the Kashi-Atushi fold system, but stands in contrast to the relatively symmetrical, box-shaped Atushi fold [*Chen et al.*, 2002, 2007; *Scharer et al.*, 2004, 2006; *Heermance et al.*, 2008] (Figure 2). One possible cause for fold asymmetry is that more rapid erosion of one fold flank promotes enhanced rock uplift of the limb that has experienced more erosional unloading [*Simpson*, 2004; *Graveleau and Dominguez*, 2008; *Graveleau et al.*, 2012]. Both Mushi and Kashi anticlines have rivers that impinge on their northern flanks and have beveled that flank down to local base level. In addition, active depositional basins are increasing the load on the southern fold flank. These divergent spatial trends of erosional unloading versus depositional loading may promote differential uplift and the observed fold asymmetry. The symmetrical Atushi fold also has a river impinging on its northern flank, but that river eroded nearly across the entire fold [*Heermance*

et al., 2008], such that unloading (and presumably any rock uplift) was of a similar magnitude across the fold's width.

[15] Total shortening is estimated from the excess area method [*Epard and Groshong*, 1993]. If folding results from a total shortening S of a unit with thickness h detached from the footwall, mass conservation implies that area A above the detachment level is

$$A = S.h \qquad (1)$$

This equation assumes that cross-sectional area is preserved during folding and out-of-the-plane transport and volume changes can be neglected. Following this approach, the depth of detachment surface and the area yield a shortening of 740 ± 110 m. The uncertainty derives mainly from the uncertainty in the depth of detachment surface. Although the topographic relief is merely ~500 m, the total structural uplift is as much as ~1300 m. The calculated total shortening and structural uplift are considered best constrained in the middle part of the fold, and they should increase westward.

4. Characteristics of Fluvial Terraces

4.1. Fluvial Terraces Description

[16] Vertical downcutting and lateral beveling by the Kezilesu River into the Mushi anticline has created flights of fluvial terraces perched across the core and most of

Table 1. OSL Dating Results (2σ) for Samples Collected From Fluvial Terraces on the Mushi Anticline

Sample No.[a]	Depth (m)	Bulk Alpha[b] (ks^{-1} cm^{-2})	K[c] (%)	SWC[d] (%)	WC[d] (%)	Dose Rate (Gy/ka)	Equivalent Dose (Gy)	Age (ka)	Related Terrace
LED09-157	1.1	5.42 ± 0.09	1.02	26	13 ± 13	2.1 ± 0.3	33.4 ± 2.4	15.7 ± 2.4	T2a
LED09-159	3.0	4.49 ± 0.08	1.04	25	13 ± 13	1.9 ± 0.2	126.6 ± 8.5	66.0 ± 9.8	T3b
LED09-160	0.6	4.76 ± 0.08	1.01	24	12 ± 12	2.1 ± 0.3	86.1 ± 6.5	42.0 ± 6.2	T3b
LED09-458	1.4	4.72 ± 0.08	1.01	24	12 ± 12	2.0 ± 0.2	112.3 ± 7.2	56.1 ± 8.0	T3b
LED09-461	2.7	4.49 ± 0.08	1.00	29	15 ± 15	1.9 ± 0.2	256.4 ± 22.8	138.4 ± 22.7	T4
LED09-462	6.2	4.23 ± 0.07	1.00	30	15 ± 15	1.7 ± 0.2	231.8 ± 16.2	133.3 ± 20.8	T4
LED09-463	2.2	4.85 ± 0.08	1.03	29	15 ± 15	2.0 ± 0.3	254.4 ± 19.5	129.9 ± 21.0	T4

[a]4–11 μm fine-grained quartz separation and measurements follow standard methods [*Li et al.*, 2012; *Lu et al.*, 2007]. Measurements were made in the State Key Laboratory of Earthquake Dynamics, Institute of Geology, China Earthquake Administration.
[b]Measured using the thick-source alpha counting technique.
[c]Measured using X-ray fluorescence.
[d]SWC stands for lab measured saturated water content of the sample. WC stands for water content assumes an average of 0% (dry sample) and measured saturated water content.

northern part of the fold (Figures 3b and 3c). All terraces are strath terraces, which were eroded into the Atushi and Xiyu Formations and are presently covered by several meters of fluvial gravels with rare silt lenses. The terrace surfaces, tightly packed with clasts and textured by small-scale paleochannels, are generally planar and relatively uneroded, except near the descending risers where transverse channels cut steeply into the underlying bedrock. The inner (southern) margins of the terraces are commonly covered by colluvial, alluvial, or aeolian deposits. Terraces preserved south of the Kezilesu River are broader and more continuous, and they contain more levels than terraces to the north of the river. This asymmetrical distribution may reflect northward migration of the Kezilesu River during the uplift of the anticline.

[17] Based on field observations and interpretation of ASTER satellite images and aerial photographs, we mapped the terraces and their underlying structure in detail (Figures 3b and 3c). Terraces can be categorized into four major divisions through field correlations that mainly refer to elevation above the present-day riverbed and to the degree of weathering of the terrace surface. Each major division contains several terrace sublevels. Among all terraces, the T2 terrace is the most spatially extensive and best-preserved terrace. It contains the T2a, with a tread elevation ~30–40 m above the riverbed, and the T2b, whose tread is ~3–5 m higher than that of the T2a. Elevations of the T1, T3a, T3b, and T4 terraces are ~5–16, ~50, ~70, and ~100 m above the riverbed, respectively.

4.2. Fluvial Terraces Chronology

[18] We rely on optically stimulated luminescence (OSL) dating to provide chronologic constraints on the terrace surfaces. OSL dating of late-Quaternary sediments can accurately reflect depositional ages, as long as the material was sufficiently exposed to sunlight prior to deposition. Seven samples were collected from silt or fine-grained sand lenses in fluvial deposits of the T2a, T3b, and T4 (Figures 3b and 5). All samples were analyzed following the sensitivity-corrected multiple aliquot regenerative-dose protocol on the 4–11 μm grain-size quartz fraction (Figure 5c) [*Lu et al.*, 2007; *Li et al.*, 2012]. Because water absorbs some part of alpha, beta, and gamma rays that contribute to the dose rate, the impact of water content was included in the dose rate calculations [*Li et al.*, 2012]. The samples had dried out before sampling but were saturated by water when deposited. We do not know, however, when they were raised above the groundwater table and became drier. In order to cover all

likely values, an average of 0% (dry) and the saturated water content (24–30%) has been utilized in age calculations. Due to the near-surface position of all samples (Table 1), it is reasonable to use the depositional OSL ages to approximate the time of terrace abandonment.

[19] Sample LED09-157, from the T2a, has an age of 15.7 ± 2.4 ka (2σ) (Table 1), similar to the Last Glacial Maximum terrace age of 18.4 ± 4.8 ka in the Mayikake basin (Figure 2a) [*Li et al.*, 2012]. Ages for LED09-159, LED09-160, and LED09-458 that were collected from the T3b terrace are 66.0 ± 9.8, 42.0 ± 6.2, and 56.1 ± 8.0 ka, respectively, spanning a wide time interval. We use their average
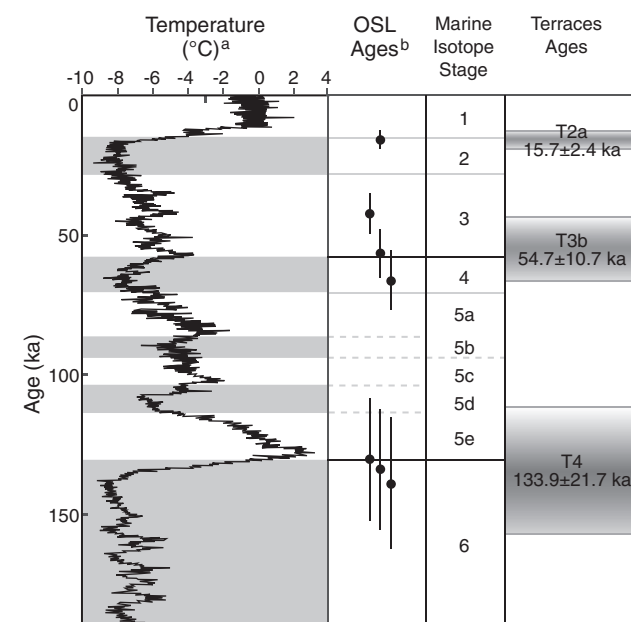

[a]Vostok ice-core record of Antarctic atmospheric paleotemperature from Petit et al. (1999).
[b]Optically stimulated luminescence ages bracketing major terrace in the Mushi anticline. Errors represent standard errors on reported ages. See text for sample locations and age interpretations.

Figure 6. Chronology of major terraces preserved on the Mushi anticline. Gradient shading bars in the right-hand column represent mean value and uncertainty (2σ) of OSL ages. OSL dates with 2σ errors (second column) of terrace deposits suggests correlation of the T2a, T3b, and T4 to transition periods of Marine Isotope Stage 2 to 1, 4 to 3, and 6 to 5e, respectively.
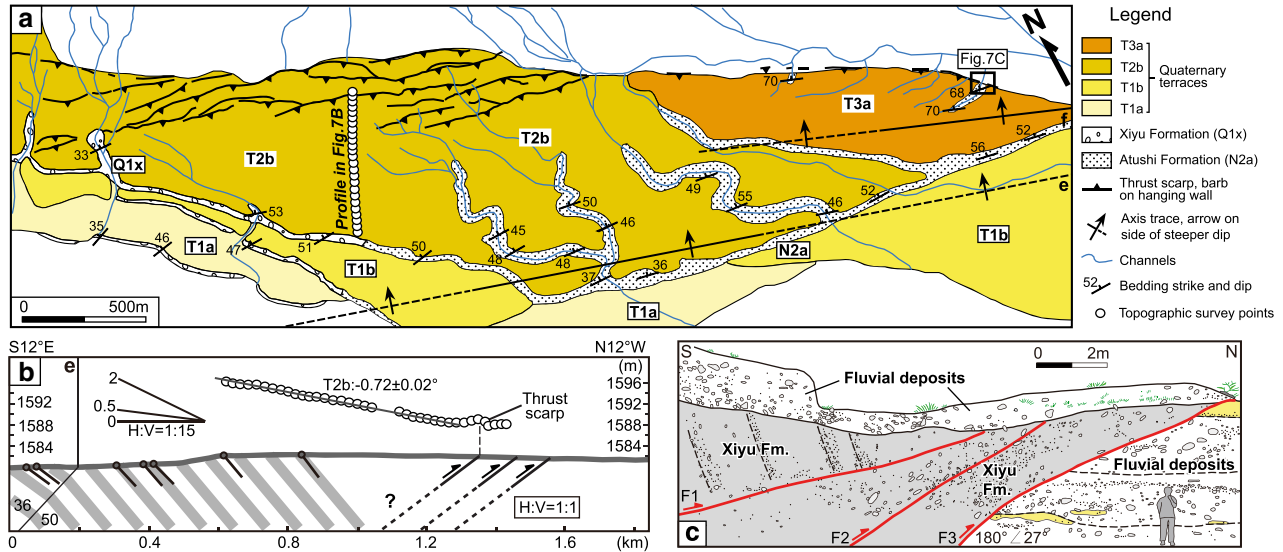
Figure 7. (a) Map of fluvial terraces lying on the northwestern Mushi anticline, as interpreted from field mapping and 1983 aerial photographs. Mapping area is shown in Figure 3b. (b) Composite survey profile (marked in Figure 7a) across terrace T2b, bedding dips, and thrust scarps. Note that change in vertical scale; and the terrace surface is back-tilted just south of the thrust scarp. Hinges e and f mark dip-domain boundaries. (c) Sketch of thrust outcrop (marked in Figure 7a) close to the dam of the Kashgar power station.

age of 54.7 ± 10.7 ka (2σ) to represent the T3b age. Samples LED09-461, LED09-462, and LED09-463 from the T4 terrace yield ages of 138.4 ± 22.7, 133.3 ± 20.8, and 129.9 ± 21.0 ka, respectively, and we used the average age of 133.9 ± 21.7 ka (2σ) as the terrace age. Ages of the T2a, T3b, and T4 can be correlated with transition intervals of Marine Isotope Stages 2 to 1, 4 to 3, and 6 to 5e, respectively (Figure 6). These correlations lend support to the increasing widespread recognition that the river incision and terrace formation coincided with major global climate changes [*Molnar et al.*, 1994; *Pan et al.*, 2003]. The interplay between enhanced water discharge (q_w) and sediment discharge (q_s) during these climate transitions is proposed to promote lateral beveling and creation of straths [*Hancock and Anderson*, 2002], especially in areas where weakly indurated strata are readily eroded. Thick terrace-mantling sediments indicate subsequent intervals when q_s/q_w increases, whereas when $q_w >/q_s$ decreases, the river tends to incise through the strath and its cover sediments to produce a lower channel flanked by paired terraces.

5. Terraces Survey and Deformation

5.1. Survey Methods and Basic Assumptions

[20] Fluvial terraces spanning the Mushi fold were clearly deformed in response to its growth (Figures 7–10). Deformation includes thrust faulting, tilting, or back-tilting perpendicular to the fold axis, and tilting parallel to the fold axis. To quantify the deformation, we surveyed terrace surfaces using an E-survey 660 Real-Time Kinematics dGPS system which yields relative vertical and horizontal precisions of <4 cm: less than the geomorphic noise due to natural ground surface irregularities. Survey lines (Figures 7–9) were roughly linear and avoided areas where the original terrace surface was mantled by young colluvial and alluvial deposits, as well as areas of subsequent erosion or artificial modification. Survey points of cross and longitudinal profiles were projected to a direction

perpendicular and parallel with the fold axis (Figures 7–10), respectively. For the riverbed and terrace T4, it is difficult to obtain continuous survey points for a longitudinal profile. We, therefore, extracted topographic points from the ASTER 30 m GDEM data (Figure 10). Terrace slopes were calculated by a least squares linear regression method. Additionally, because the surface deformation is related to the underlying structures, bedding dips were also projected perpendicular to the fold axis, such that the dips presented are apparent dips (Figures 7 and 8).

[21] The initial gradient of terrace surfaces provides a reference frame that is used to determine how the surfaces were deformed due to folding. We assume that all terrace surfaces formed with a gradient similar to the modern Kezilesu riverbed. Survey lines cp7 and lp0 indicate transverse and longitudinal gradients of the modern riverbed are $-0.01° \pm 0.01°$ and $-0.36° \pm 0.02°$, respectively (Figures 8 and 10); each representing the initial cross-section slopes and longitudinal slopes of all terrace surfaces. (Note that along cross profiles, terrace surfaces that slope, tilt, or rotate downward to the south are defined as positive, whereas tilts to the north are defined as negative; along longitudinal profiles, terrace surfaces that slope, tilt, or rotate to the east are defined as negative).

5.2. Terrace Deformation

[22] The northwestern region of the anticline (Figure 7a) is capped by smooth T2b and T3a terraces, as well as by younger, vegetation-covered, and uneven T1a and T1b terraces. Underlying bedrock, exposed by deep incision from modern ephemeral channels that cut into the edges of terrace risers, reveals ESE-trending hinges. The northern margins of T2b and T3a are defined by a series of subparallel ENE-trending thrust scarps (Figure 7a), which prevent southward transport of alluvial deposits from the Mingyaole anticline. Field mapping and interpretations of 1983 aerial photographs indicate that the western part of thrust scarps includes 3–6 splays, with heights ranging 0.4–3.4 m [*Chen et al.*, 1997]. Near the dam of
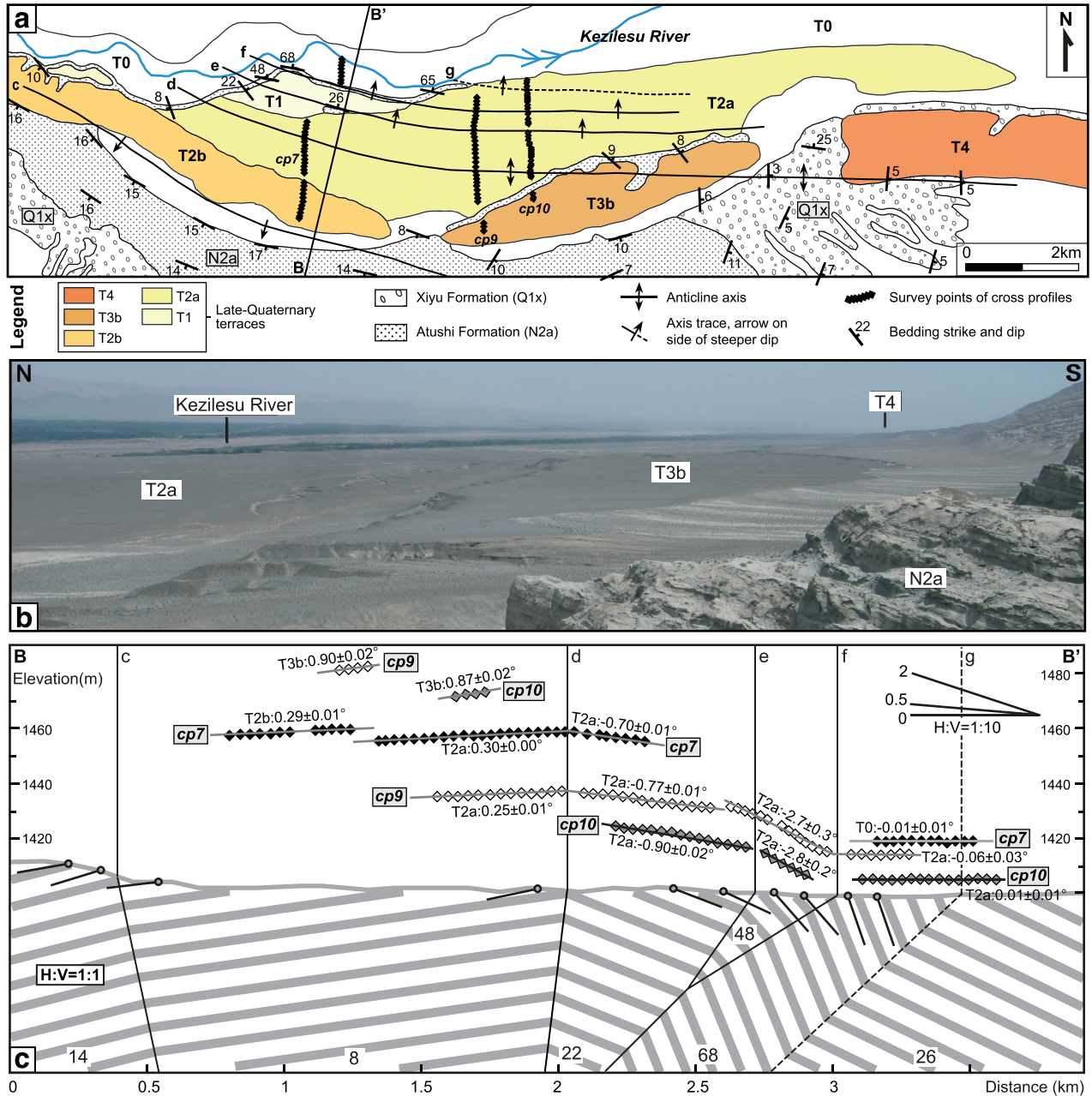
Figure 8. (a) Map interpreted from the ASTER satellite images and survey profiles of fluvial terraces lying on northern part of the Mushi anticline. The map area is shown in Figure 3b. Hinge c, d, e, f, and g mark dip-domain boundaries. (b) Photograph of major fluvial terraces. (c) Survey profiles of terraces across the fold and bedding dips close to structural section B-B′ (marked in Figure 8a). Note that above the surface, survey profiles are shown with 10× vertical exaggeration. Notably, the tilt direction of terraces is consistent with the dip direction of pregrowth strata and that the terrace surfaces are kinked only at the fold hinges.

the Kashgar power station, steep, gray-black Xiyu Formation overthrusts subhorizontal terrace deposits along a ~6 m thick fracture zone that comprises three faults that are recognizable by the alignment of gravel clasts (Figures 7a and 7c). The F1 and F2 faults terminate under terrace deposits, suggesting that slip on them had already ceased before terrace abandonment. The F3 fault, with a dip direction/dip of 180°/27°, displaces the terrace deposits, creating a ~4.6 m high scarp on the terrace surface. South of the thrust scarps, the T2b terrace displays slight back-tilting away from the riverbed (Figure 7b).

[23] In the middle and eastern parts of the anticline (Figure 8), the terrace surfaces have been folded across the growing anticline. Close to the section B-B′, terraces T3b and the southern segment of the T2 are back-tilted ~0.9° and ~0.26°–0.37°, respectively, along profiles cp6–cp10 (Figures 8c and 9), thereby exhibiting a progressive increase in dip with age. Through axis d, which separates the 8°S and 22°N dip domains, terrace T2a tilts ~ −0.7°–0.9° toward the river and its surface displays a gentle curve. The steepest terrace slopes (~−2.8° tilt) in the anticline

4636
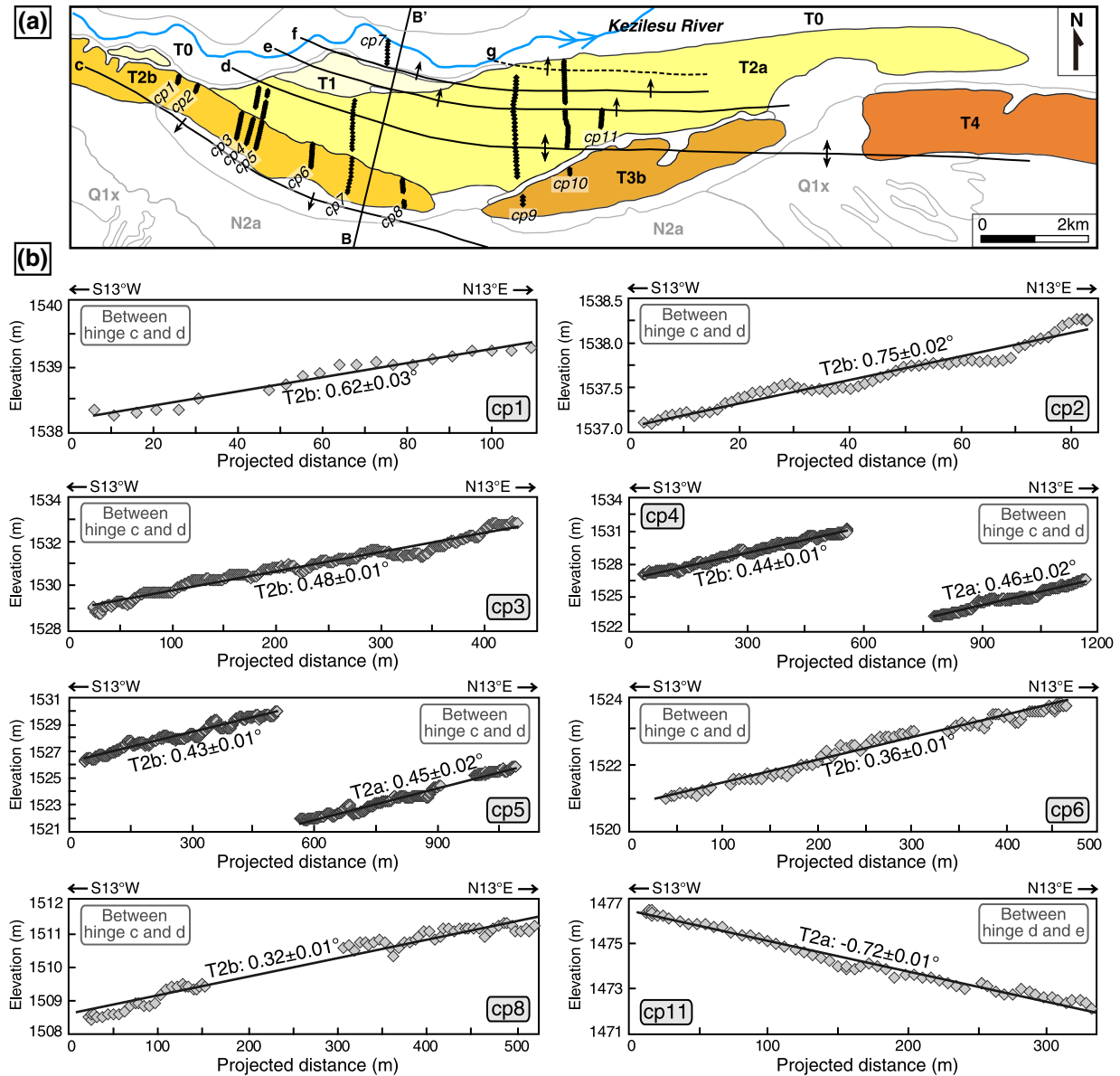
Figure 9. Differential GPS survey profiles and surface slopes from linear regressions across deformed fluvial terraces preserved on the northern Mushi anticline. (a) The map (for legend, see Figure 8a) shows the locations of these profiles. (b) Differential GPS survey profiles.

are located above bedrock that dips 48°N (between hinge e and f). North of the hinge f, parallelism between the T2a terrace and the modern riverbed suggests that rotation of the domain dipping 68°N has stopped since the terrace was abandoned.

[24] Along strike, each terrace surface has notably different rotation angles from west to east (Figures 8c, 9, and Table 2). For the T2b and southern segment of the T2a terrace, located on the bedrock dipping 8°S (between hinges c and d), rotation angles approximately decrease from ~0.8° to ~0.3° and from ~0.5° to ~0.3°, respectively. This eastward tendency toward gentler slopes appears to correlate with the steeper and tighter shape of the western part of the Mushi anticline and can be attributed to eastward growth of the fold.

[25] The fluvial terraces are deformed not only in cross profiles perpendicular to the fold axis but also in longitudinal

profiles parallel to the fold axis (Figure 10). According to the dGPS survey points and extracted data from ASTER satellite GDEM data, the southern part of the T2a, T3b, and T4 terraces tilt −0.10° ± 0.03° (2σ) (profile lp2″ and lp2‴), −0.54° ± 0.02° (profile lp3), and −0.89° ± 0.05° (profile lp4), respectively, compared to the riverbed, and they, therefore, exhibit age-dependent increases in slope. On average, these terraces display a rather steady rate of differential tilting of ~0.08°/ka parallel to the fold's strike. This tilting is interpreted to represent lateral rotation during the fold's evolution. The western part of the T2a terrace along the lp2′, however, has a slope similar to the modern riverbed, indicating that no differential uplift occurred in this zone. This absence of differential uplift is consistent with the rotation ceasing within dip domain 68°N since T2a was abandoned. If the current surface slope along lp2′ is interpreted as the original T2a slope at the time
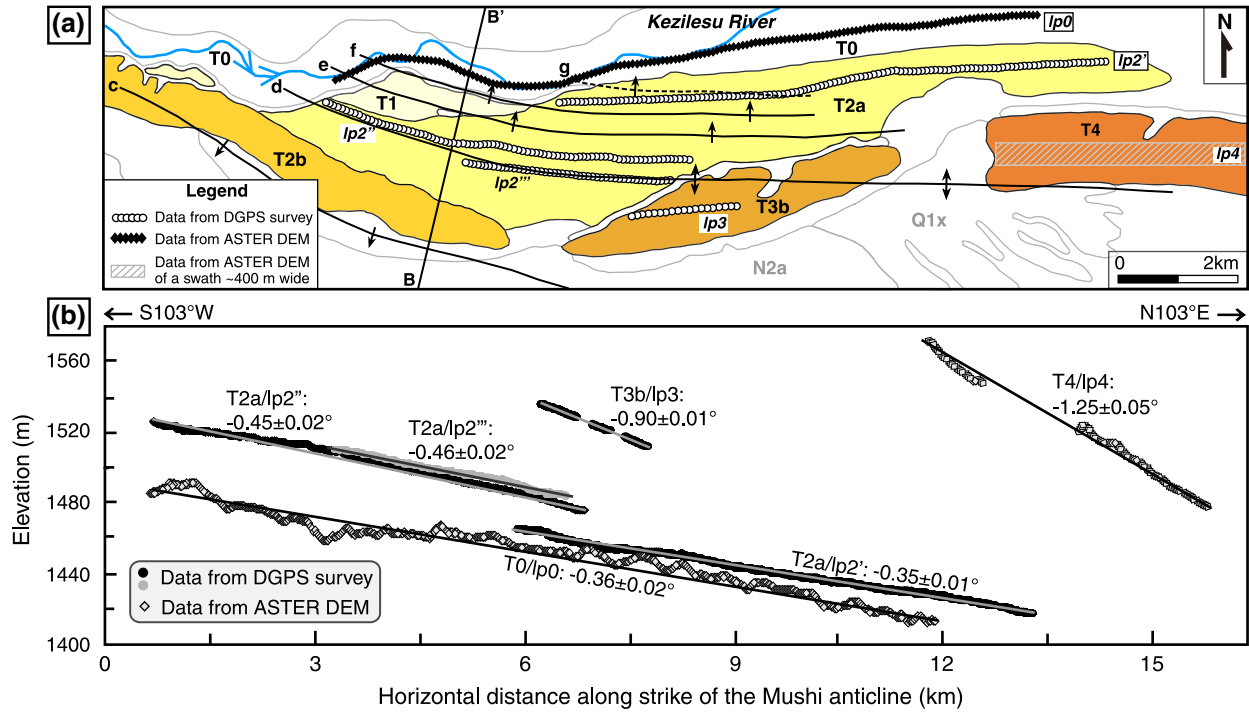
Figure 10. Longitudinal profiles along fluvial terraces preserved on the northern Mushi anticline projected on to a N103°E line. (a) The map (the legend refers to Figure 8a) shows the locations of these profiles. (b) Longitudinal profiles. The "noisy" profile lp0 of the riverbed is extracted from the 30 m ASTER GDEM dat. Its variable distance from the projection direction and fold axis affects its apparent slope. The profile lp4 is from the average elevation of the ASTER GDEM in a swath ~400 m wide. Other profiles are from dGPS surveys. These profiles exhibit a progressive increase in rotation angle with age.

of abandonment, it implies the riverbed slope has remained constant since ~16 ka. The parallelism of the T2a with the modern river appears to validate the basic assumption that the original gradients of terrace surfaces were similar to that of the modern Kezilesu riverbed.

6. Shortening, Uplift, and Rates

[26] Deformed fluvial terraces have been used to constrain thrust-related folding in fault-bend folds [*Lavé and Avouac*, 2000; *Thompson et al.*, 2002; *Hubert-Ferrari et al.*, 2007], fault-propagation folds [*Bullard and Lettis*, 1993;

Table 2. Rotation Angles in Cross Profiles of Fluvial Terraces and Associated Parameters for Calculating Incremental Shortening in Equation (2)–(5)

Terrace	Distance[a] (km)	θ_i (°)	z (km)	S (m)	β_i[b] (°)	W[b] (km)	$\lambda(z)$[b] ($10^{-4} \cdot m^{-1}$)	s (m)	Survey Profile
T2a	2.05	0.47 ± 0.02	7.5 ± 1.0	740 ± 110	8.0 ± 0.8	8.5 ± 0.9	1.2 ± 0.1	$45.9+16.9/-10.2$	cp4
T2a	2.22	0.46 ± 0.02	7.5 ± 1.0	740 ± 110	8.0 ± 0.8	8.5 ± 0.9	1.2 ± 0.1	$44.8+16.7/-9.7$	cp5
T2a	3.8	0.31 ± 0.01	7.5 ± 1.0	740 ± 110	8.0 ± 0.8	8.5 ± 0.9	1.2 ± 0.1	$30.2+11.0/-6.5$	cp7
T2a	7.0	0.26 ± 0.01	7.5 ± 1.0	740 ± 110	8.0 ± 0.8	8.5 ± 0.9	1.2 ± 0.1	$25.4+9.3/-5.5$	cp9
T2a	3.8	-0.69 ± 0.01	7.5 ± 1.0	740 ± 110	-22.0 ± 2.2	8.5 ± 0.9	1.2 ± 0.1	$23.5+8.1/-5.0$	cp7
T2a	7.0	-0.76 ± 0.01	7.5 ± 1.0	740 ± 110	-22.0 ± 2.2	8.5 ± 0.9	1.2 ± 0.1	$25.9+8.9/-5.5$	cp9
T2a	7.7	-0.89 ± 0.02	7.5 ± 1.0	740 ± 110	-22.0 ± 2.2	8.5 ± 0.9	1.2 ± 0.1	$30.3+10.6/-6.6$	cp10
T2a	8.3	-0.71 ± 0.01	7.5 ± 1.0	740 ± 110	-22.0 ± 2.2	8.5 ± 0.9	1.2 ± 0.1	$24.3+8.2/-5.2$	cp11
T2a	7.0	-2.7 ± 0.3	7.5 ± 1.0	740 ± 110	-48.0 ± 4.8	8.5 ± 0.9	1.2 ± 0.1	$32.4+20.3/-11.0$	cp9
T2a	7.7	-2.8 ± 0.2	7.5 ± 1.0	740 ± 110	-48.0 ± 4.8	8.5 ± 0.9	1.2 ± 0.1	$34.0+13.3/-10.9$	cp10
T2b	0.5	0.63 ± 0.03	7.5 ± 1.0	740 ± 110	8.0 ± 0.8	8.5 ± 0.9	1.2 ± 0.1	$60.6+27.8/-14.3$	cp1
T2b	0.89	0.76 ± 0.02	7.5 ± 1.0	740 ± 110	8.0 ± 0.8	8.5 ± 0.9	1.2 ± 0.1	$73.2+32.7/-16.8$	cp2
T2b	1.8	0.49 ± 0.01	7.5 ± 1.0	740 ± 110	8.0 ± 0.8	8.5 ± 0.9	1.2 ± 0.1	$47.3+20.8/-10.8$	cp3
T2b	2.05	0.45 ± 0.01	7.5 ± 1.0	740 ± 110	8.0 ± 0.8	8.5 ± 0.9	1.2 ± 0.1	$43.4+19.4/-9.9$	cp4
T2b	2.22	0.44 ± 0.01	7.5 ± 1.0	740 ± 110	8.0 ± 0.8	8.5 ± 0.9	1.2 ± 0.1	$42.5+19.0/-9.7$	cp5
T2b	3.2	0.37 ± 0.02	7.5 ± 1.0	740 ± 110	8.0 ± 0.8	8.5 ± 0.9	1.2 ± 0.1	$35.7+16.5/-8.7$	cp6
T2b	3.8	0.30 ± 0.02	7.5 ± 1.0	740 ± 110	8.0 ± 0.8	8.5 ± 0.9	1.2 ± 0.1	$29.0+13.9/-7.3$	cp7
T2b	4.6	0.33 ± 0.02	7.5 ± 1.0	740 ± 110	8.0 ± 0.8	8.5 ± 0.9	1.2 ± 0.1	$31.8+14.9/-7.7$	cp8
T3b	7.0	0.91 ± 0.02	7.5 ± 1.0	740 ± 110	8.0 ± 0.8	8.5 ± 0.9	1.2 ± 0.1	$87.5+38.4/-19.9$	cp9
T3b	7.7	0.88 ± 0.02	7.5 ± 1.0	740 ± 110	8.0 ± 0.8	8.5 ± 0.9	1.2 ± 0.1	$84.4+37.2/-19.0$	cp10

[a]Distance means relative distance of cross profile along strike of the fold.
[b]Errors of pregrowth strata dip (β_i), the fold's width (W), and related $\lambda(z)$ assume ±10%.
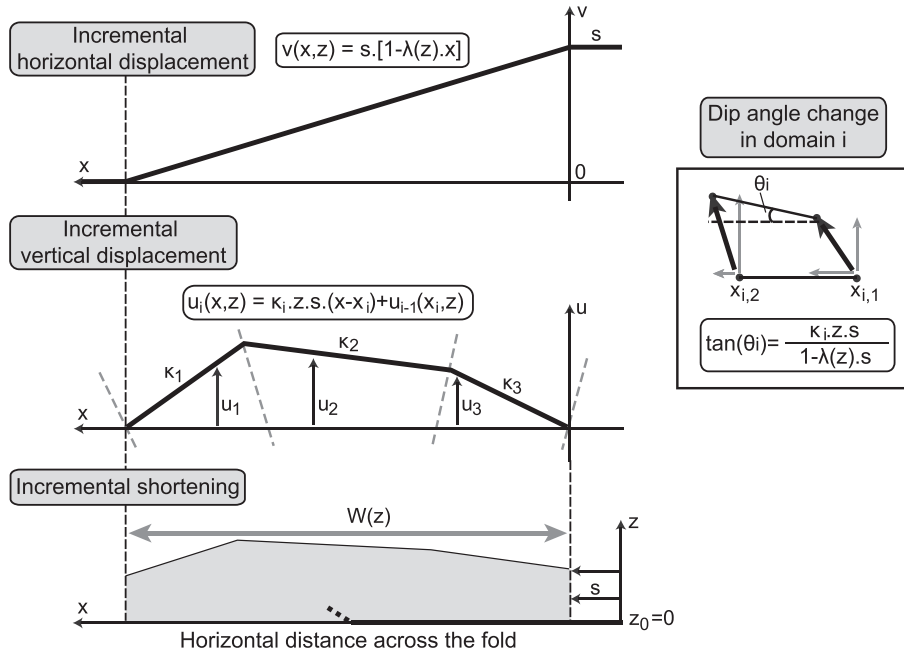
Figure 11. Sketch illustrating the relationship of incremental horizontal displacement (v) and incremental vertical displacement (u) to incremental shortening (s), according to the pure-shear fold model of *Bernard et al.* [2007], as expressed by equations (2) and (3). Inset on right illustrates relationship of dip angle θ acquired in a dip domain i to the incremental shortening s as a function of the model parameters (κ_i and λ) and of the elevation above the detachment (z) as expressed by equation (4). Modified from *Simoes et al.* [2007].

Benedetti et al., 2000], detachment folds [*Rockwell et al.*, 1988; *Scharer et al.*, 2006], and listric thrust folds [*Amos et al.*, 2007]. Recently, *Bernard et al.* [2007] described a kinematic model of pure-shear fault-tip folds (including fault-propagation folds and detachment folds developed above fault tips) derived from a sandbox experiment, and *Daëron et al.* [2007] and *Simoes et al.* [2007] investigated how to use this model to constrain a fold's shortening rate and uplift rate, thereby providing a simpler and more readily applicable method. Because different calculation methods are closely related to a fold's deformation style, it is critical to properly classify the fold before selecting an appropriate method.

[27] With respect to the nature of folding of the Mushi anticline, three basic observations can be made regarding the fluvial terraces on its northern half (Figures 8 and 9). First, in each cross profile, terrace surfaces are discordant with the bedding into which they were beveled, but dip directions of tilted terraces and underlying strata are consistent. Second, terrace surfaces display increasing dips with age. Third, terrace elevations are highest in the fold's core and decrease toward its limbs. These observations indicate that the fold is not raised as a uniform block as predicted by hinge migration; instead, it grows by progressive rotation of the limbs. Therefore, it appears that the Mushi anticline is a fault-tip fold formed by limb rotation resulting from pure shear. Although it cannot be completely ruled out, kink-band migration appears negligible because no fold scarp was found on the alluvial fans in the southern limb or on the terrace surfaces in the northern limb [*Hubert-Ferrari et al.*, 2007]. We favor the pure-shear fault-tip fold model [*Bernard et al.*, 2007; *Daëron et al.*, 2007; *Simoes et al.*, 2007] to calculate the shortening rate and uplift rate.

6.1. Shortening and Uplift Calculation of Pure-Shear Fault-Tip Folds

[28] In the sandbox experiment [*Bernard et al.*, 2007], key observations are that the horizontal velocity varies linearly across the whole fold and that the uplift rate varies linearly within domains separated by hinges (Figure 11). The incremental horizontal displacement $v(x,z)$ resulting from an increment of shortening s is a linear function of horizontal distance x between the first and last hinge of a fold, whereas the incremental vertical displacement $u_i(x,z)$ is also a linear function of x within each domain i defined by two hinges:

$$v(x,z) = s.[1 - \lambda(z).x]; \qquad (2)$$

$$u_i(x,z) = k_i.z.s.(x - x_i) + u_{i-1}(x_i,z), \qquad (3)$$

where z is the elevation above the detachment surface, $\lambda(z) = 1/W(z)$ with $W(z)$ being the width of the fold at elevation z, κ_i is a parameter characteristic of domain i as defined below, and x_i is the horizontal position of the axial line separating domains i and $i-1$. The term $u_{i-1}(x_i,z)$ is the incremental uplift at the point of coordinate (x_i, z) along the axial line, and it ensures continuity of vertical displacements between domains. Deformation by pure shear allows for limb rotation during folding. Within the domain i, the change in dip angle θ_i associated with incremental shortening s is given from equations (2) and (3):

$$\tan\theta_i = \frac{\kappa_i.z.s}{1 - \lambda(z).s}. \qquad (4)$$

In domain i, given input of (i) pregrowth strata with dip β_i (originally at altitude z), (ii) a fluvial terrace with

Table 3. Incremental Shortening and Incremental Uplift and Associated Parameters (Other Parameters Used in the Equations (3)–(5) Referring to Table 2), as Well as OSL Ages of Terraces

Terrace	θ_i[a] (°)	β_i[b] (°)	β_1[b] (°)	β_2[b] (°)	β_3[b] (°)	x_2-x_1 (km)	x_3-x_2 (km)	x_4-x_3 (km)	s (m)	u (km)	OSL Age (ka)
T2a	0.29 ± 0.03	8.0 ± 0.8	8.0 ± 0.8	14.0 ± 1.4	8.0 ± 0.8	2.3 ± 0.2	2.7 ± 0.3	1.9 ± 0.2	$28.2+12.7/-7.6$	$44.1+18.1/-11.5$	15.7 ± 2.4
T2a	-0.78 ± 0.06	-22.0 ± 2.2	8.0 ± 0.8	14.0 ± 1.4	8.0 ± 0.8	2.3 ± 0.2	2.7 ± 0.3	1.9 ± 0.2	$24.7+10.0/-5.8$	$38.7+14.5/-8.6$	15.7 ± 2.4
T2a	-2.8 ± 0.3	-48.0 ± 4.8	8.0 ± 0.8	14.0 ± 1.4	8.0 ± 0.8	2.3 ± 0.2	2.7 ± 0.3	1.9 ± 0.2	$32.9+17.0/-10.0$	$51.6+25.3/-15.1$	15.7 ± 2.4
T3b	0.90 ± 0.03	8.0 ± 0.8	8.0 ± 0.8	14.0 ± 1.4	8.0 ± 0.8	2.3 ± 0.2	2.7 ± 0.3	1.9 ± 0.2	$88.4+31.1/-18.7$	$137.6+57.8/-36.9$	54.7 ± 10.7

[a]Average rotation angles along profiles cp5 and cp7 close to the structural cross-section B-B′ are used.
[b]Errors of pregrowth strata dip (β_i) and dip domain i width ($x_{i+1}-x_i$) of pregrowth strata assume ±10%.

rotation angle θ_i (originally at the same altitude z), and (iii) total shortening S, incremental shortening s can be estimated according to equation (4):

$$s = \frac{\tan(\theta_i).S}{\tan(\beta_i).(1 - \lambda(z).S) + \tan(\theta_i).\lambda(z).S}. \quad (5)$$

[29] *Bernard et al.* [2007] and *Simoes et al.* [2007] also proposed an approach to test the consistency of a fold's deformation with this calculation method. According to equation (4), $[\tan(\theta_i).(1-\lambda(z).s)]/s$ should be a linear function of z. We can check this predicted consistency if the total shortening S, z, and the related dip angle β_i of pregrowth strata in the domain i can be determined through mapping data and seismic reflection data. For the Mushi anticline, we do not know β_i well enough due to the limited extent of bedrock outcrop and the lack of seismic reflection profiles to implement this consistency test. Here we propose a new approach based on equation (4). If a fluvial terrace, e.g., the T2a in the Mushi anticline (Figure 8), overlies more than one domain, the terrace's rotation angle θ_{i-1} and underlying bedding dip angle β_{i-1} in domain $i-1$, and β_i and θ_i in domain i should follow this relation:

$$\frac{\tan(\theta_{i-1})}{\tan(\beta_{i-1})} = \frac{\tan(\theta_i)}{\tan(\beta_i)} = \text{constant}. \quad (6)$$

This relation implies that the part of a terrace overlying a steeper bedrock domain should be rotated by a larger angle during distributed pure-shear folding than a terrace segment overlying a gentler dipping bedrock domain.

### 6.2. Determination of Shortening, Uplift, and Rates

[30] Initially, we tested whether deformation of the Mushi anticline fits the consistency requirement for the above method. For T2a, profiles cp7, cp9, and cp10 lie close to the structural section B-B′ and cross four dip domains (Figure 8). In dip domains 8°S, 22°N, and 48°N, the average rotation angles are $0.29°\pm0.03°$, $-0.78°\pm0.06°$, and $-2.8°\pm0.3°$, and the related $\tan(\theta_i)/\tan(\beta_i)$ ratios (from equation (6)) are 0.036 ± 0.005, 0.034 ± 0.005, and 0.044 ± 0.009, respectively, which we regard as roughly equal. For the domain 68°N, however, the rotation angle of T2a is nearly 0°, much smaller than the model prediction of ~$-4.4°$–$6.0°$. This discrepancy may be attributed to strong strain localization and nonpure-shear deformation that apparently occurred in the domain 68°N. Such strain localization is common in the frontal-most area of a fold [*Simoes et al.*, 2007]. An alternative interpretation is that the domain 68°N is related to active

faulting such that hinge f could be localized along a reverse fault zone that is at different stages of maturity along the fold: mature to the west (fault reaches the surface), incipient in the center, and blind to the east (Figures 3 and 7). Despite this discrepancy, it appears reasonable to use this calculation method to provide a first-order approximation of incremental shortening and incremental uplift, given that the other three domains have roughly equal ratios.

[31] Parameters used in equations (5), (4), and (3) were determined using the available data (Table 3). Rotation angles (θ_i) of T2a and T3b were extracted from profiles cp7, cp9, and cp10, close to the structural cross-section B-B′ (Figure 8). The vertical distance, z, of T2a and T3b to the detachment surface close to the axis d in Figure 4 is about 7.5 ± 1 km, the width (W) of the fold at the elevation z above the detachment surface is 8.5 ± 0.9 km, and the total shortening (S) of the anticline is 740 ± 110 m. The increments and rates of shortening and uplift are presented with the most probable value and minimum and maximum 95% confidence values resulting from Monte Carlo simulations of uncertainties (see Appendix A). Combining above parameters and OSL ages of T2a and T3b, the shortening rate and uplift rate are $1.5+1.3/-0.5$ mm/a and $2.3+2.1/-0.8$ mm/a, respectively
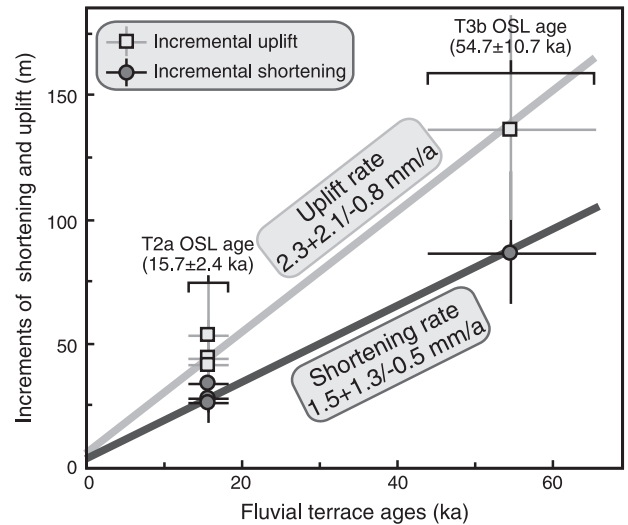
Figure 12. Incremental shortening and uplift versus OSL ages of fluvial terraces surveyed in the field, which gives a roughly uniform shortening rate and uplift rate since abandonment of T3b. Three incremental shortening and uplift magnitudes can be separately calculated from the terrace's average rotation angle in domains 8°S, 22°N, and 48°N along profiles cp7, cp9, and cp10 (Figure 8).
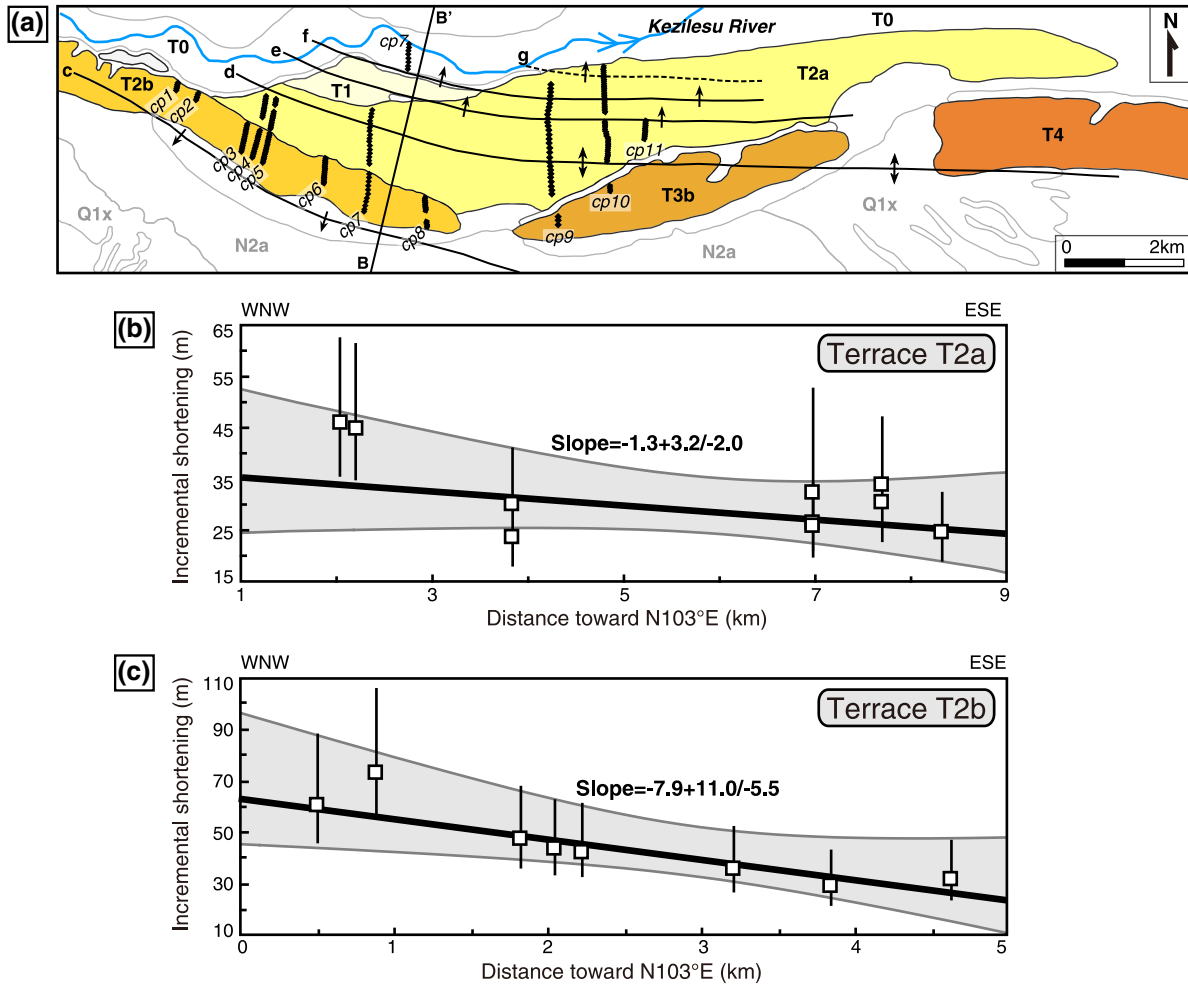
Figure 13. Linear trends interpreted to result from incremental shortening along strike of the Mushi anticline since abandonment of terraces T2a and T2b. (a) The map (the legend refers to Figure 8a) shows the locations of these profiles. (b and c) The incremental shortening is calculated from rotation angles of survey profiles cp1–cp11 (shown in the top map, for legend, see Figure 8a), as well as other parameters (Table 2), based on equation (5). The gray shaded areas are 95%-error envelope. The slopes are calculated using the Monte Carlo simulations.

(Figure 12). The higher uplift rate than shortening rate is typical of pure-shear fault-tip folding: a characteristic that further supports our preferred model. If both rates were uniform through the entire folding history, the initiation age of the Mushi anticline would be ~0.5 Ma, consistent with the age deduced from the conformable contact between the Xiyu Formation and the Atushi Formation [*Chen et al.*, 2005]. This age estimate indicates the Mushi anticline is much younger than the Mingyaole and Kashi anticlines to the north (Figure 2a) [*Chen et al.*, 2005, 2007] but is consistent with the initiation age ~0.35 Ma [*Li et al.*, 2012] of the Tuomuluoan anticline that lies immediately to its west and overthrusts the southern limb of the Mingyaole anticline.

[32] Along strike of the fold, rotation angles in cross profiles of each terrace (T2a and T2b) in the same dip domain decrease from west to east (Table 2). We propose this change may reflect a decrease of incremental shortening along the fold. Assuming the total shortening and dip of underlying bedding remain roughly constant along the distance from profiles cp1 to cp11, we can estimate the incremental shortening

related to each profile since the abandonment of T2b: a terrace that exhibits a roughly linear decrease in elevation and incremental shortening from west to east (Figures 10, 13, and Table 2). Although the relationship is not as clear on T2b, the incremental shortening on T2a since its abandonment also displays a tendency for a linear decrease (Figure 13 and Table 2).

[33] Geodetic GPS data from the WUPA station southeast of the Aismaola anticline and the KSH station south of the Kashi anticline indicate a present-day convergent rate across the ~42 km wide swath between two stations (Figure 2a) [*Zubovich et al.*, 2010]. Our calculations suggest that about one half of this rate is absorbed by the Mushi anticline, and the other half may be absorbed by the Aismaola anticline, the syncline between the Aismaola anticline and the Mushi anticline, as well as the syncline between the Mushi anticline and the Kashi anticline (Figure 2a). Compared with deformation along the Pamir Frontal Thrust in the neighboring the Mayikake basin (Figure 2a), where Quaternary shortening rates of ~5–7 mm/a are concentrated in a swath less than
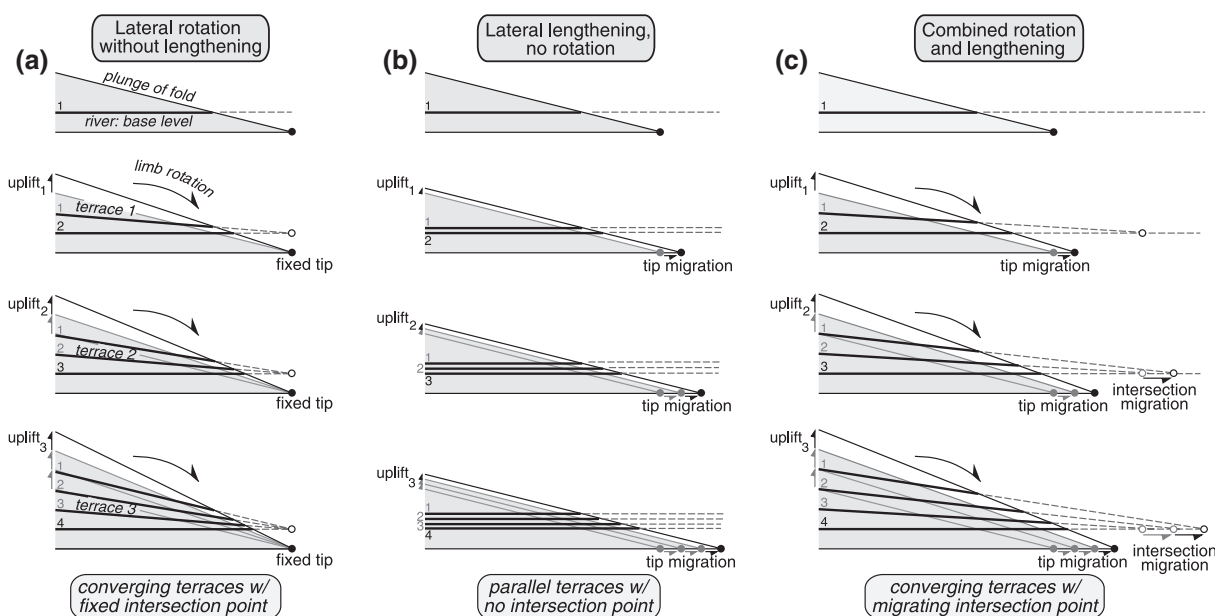
Figure 14. Kinematic models of terrace deformation along a fold's axis. Fold is shown by the gray shaded area, and the most recent growth due to lateral growth is shown by white area. Thick black lines represent terrace surfaces. Gray and black solid circles represent end points of the fold before and after lateral lengthening, respectively, and gray and black open circles represent intersection points between terrace surfaces (or linear extension) with the riverbed. The models were made assuming that uplift of the terrace surface is equal to the incremental uplift of the fold since the terrace surface abandonment. In this assumption, when the incremental plunge angle is zero, the rotation angle of the terrace surface is zero too; however, when the incremental plunge angle is larger than zero, it is slightly smaller than the rotation angle of the terrace surface due to the difference in height between river base level and fixed fold tip. (a) Rotation without lengthening. Terrace surfaces are not parallel, the older terraces have larger rotation angles, and the intersection points of terraces (or linear extension) with the riverbed (or its extension line) are closely distributed with each other and, assuming a constant local base level through time, cannot exceed end points of the fold. (b) Lateral growth solely by lengthening (no rotation). Terrace surfaces and riverbed are parallel with each other. (c) Combined lengthening and rotation. Terrace surfaces are not parallel, the intersection points of terraces (or linear extension) with the riverbed (or its linear extension) will exceed end points of the fold, and older terraces have move distant intersection points with the riverbed.

10 km wide [*Li et al.*, 2012], deformation at the longitude of the Mushi anticline is widely distributed between the Atushi-Kashi fold system [*Scharer et al.*, 2006] and the Mushi anticline: an area with a width >45 km (Figure 2a).

7. Lateral Growth

7.1. Lateral Lengthening and Rotation

[34] Lateral growth of a fold can occur by lateral lengthening, whereby a fold's tips migrate outward with constant plunge angle (Figure 14b). Alternatively, if the tips of a fold are pinned or fixed, fold growth may be accommodated by differential uplift and rotation by which a fold's plunge angle increases (Figure 14a). Quite commonly some combination of both mechanisms occurs during fold growth (Figure 14c) [*Keller et al.*, 1999; *Manighetti et al.*, 2001; *Schlagenhauf et al.*, 2008]. In the beginning stage, a fold may be dominated by lateral lengthening such that it migrates outward quickly [*Chen et al.*, 2007], whereas lateral rotation may play an increasingly important role as lengthening slows [*Amos et al.*, 2010]. In its later stages, the fold may grow merely by lateral rotation with a fixed fold length.

[35] Geomorphic criteria, suggested by *Keller et al.* [1999], can be a useful way to demonstrate a fold's lateral growth. Several structural and geomorphic characteristics of the Mushi anticline indicate its predominantly eastward growth over time. First, in the northwestern part of the fold, deformation includes thrust faulting and tilting, whereas in the middle and eastern parts, deformation includes only tilting, without any faulting. This contrast may reflect stronger strain localization in the western part due to its earlier inception. Second, in the middle and eastern parts, rotation angles of each terrace in the same domain systematically decrease from west to east. Finally, along a longitudinal direction parallel to the fold axis, fluvial terraces dip eastward more steeply than the modern riverbed slope.

[36] Such geomorphic criteria can constrain a fold's lateral growth direction and even its relative rate in certain situations [*Keller et al.*, 1998, 1999]. It is, however, commonly difficult to quantify the magnitude and rate of lateral rotation or to distinguish which mechanism plays a more important role. Terrace deformation along the fold axis makes such quantification and distinction much easier. Assuming that cumulative and incremental uplift along the fold axis accumulates linearly along strike, then the plunge
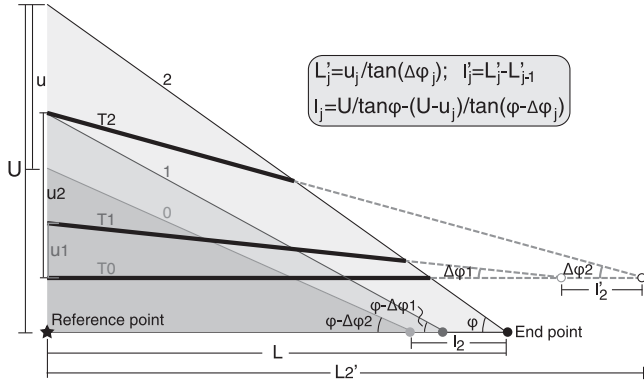
Figure 15. Sketch showing the relationship between uplift and rotation of a terrace surface along a fold's axis when accompanied by incremental lengthening of the fold. The gray shaded area depicts the fold, and the darker to lighter shading represents lateral lengthening and vertical growth from early to late stages in the folding history. Terrace surfaces (T1 and T2) and the modern riverbed (T0) are shown by thick black lines. From the reference point to the fold tip, the fold has uniform plunge angles for a given stage. At the reference point, incremental uplift u_i of the fold is equal to uplift at the same point of the terrace surface. Considering the rotation angle of the terrace surface is commonly very small (in the Mushi anticline, it is smaller than ~1.5°), the incremental plunge angle of the fold can be equalized to it.

angle of the fold can be viewed as constant toward the fold tips, and the pristine shape along the fold's crest can be viewed as linear (Figure 14). In lateral lengthening (with no rotation), terrace surfaces and the riverbed along the fold axis remain parallel with each other through time (Figure 14b). In lateral rotation (with no lengthening), terrace surfaces diverge such that older terraces have steeper slopes and larger rotation angles. In addition, the terrace surfaces (or their linear extension) should approximately intersect at a common point whose position should not exceed the fold's end point, assuming a constant local base level through time (Figure 14a). Quite commonly, during fold growth, both lengthening and rotation occur. In this case, the terrace surfaces are not parallel, but the intersection points of the terrace surfaces with the riverbed will exceed the fold's end point, and older terraces should have more distant intersection points than younger ones (Figure 14c). The distance (L_j') from a reference point to intersection point of the terrace T_j and the distance (l_j') from the intersection point of T_j to that of T_{j-1} can be estimated using the following formulas (Figure 15):

$$L_j' = \frac{u_j}{\tan\left(\Delta\varphi_j\right)}; \tag{7}$$

$$l_j' = L_j' - L_{j-1}', \tag{8}$$

where u_j is uplift of terrace T_j at the reference point and is equal to incremental uplift of the fold since abandonment of T_j, and $\Delta\phi_j$ is the rotation angle along the fold axis of T_j since abandonment. According to equations (7) and (8), if $L_j' \approx L$ or $l_j' \approx 0$, the fold propagates entirely by lateral rotation without

lengthening; if $L_j' > L$ or $l_j' > 0$, the fold grows laterally by combining lengthening with rotation, and the incremental length (l_j) can be estimated by (Figure 15):

$$l_j = \frac{U}{\tan\varphi} - \frac{U - u_j}{\tan\left(\varphi - \Delta\varphi_j\right)}, \tag{9}$$

where U is the fold's total uplift and φ is the plunge angle of the fold. Here $\Delta\varphi_j$ is the incremental plunge angle of the fold, which is equal to the rotation angle of T_j along the fold axis. Generally, the plunge angle φ cannot be calculated in a straightforward manner, but its mean value can be estimated from the formula:

$$\overline{\varphi} = \arctan\left(\frac{U}{L}\right). \tag{10}$$

If the fold propagates entirely by lateral lengthening without rotation, the above equation can be simplified to:

$$l_j = \frac{u_j}{\tan\left(\overline{\varphi}\right)}. \tag{11}$$

7.2. Lateral Growth Mechanism and Rate of the Mushi Anticline

[37] For the Mushi anticline, the dip angles of the underlying bedding are very similar (3°E–5°E) in the eastern part of the fold (Figure 3c). Longitudinal profiles of terrace surfaces that were surveyed subparallel with the fold axis are roughly linear (Figure 10), indicating a tendency toward a linear gradient of uplift of terrace surfaces along the fold axis with time. If so, we can use the above model to define the deformation mechanisms of the anticline. Based on the longitudinal profiles lying subparallel to the fold axis (Figure 10), the lateral rotation angles ($\Delta\varphi_i$) of T2a, T3b, and T4 are $-0.10° \pm 0.03°$, $-0.54° \pm 0.02°$, and $-0.89° \pm 0.05°$, respectively, and exhibit increased angles with age. Therefore, lateral rotation clearly occurred during the fold's growth. Given that incremental uplift since abandonment of T2a and T3b have been estimated and that incremental uplift of the T4 can be calculated assuming that the uplift rate is constant (Table 4), we can use equations (7) and (8) to estimate the distance (L') from the structural cross-section B-B′ (or A-A′) (Figure 10) to the intersection points of the terrace T_j with the modern riverbed and the distance (l_j') between any two terraces' intersection points (Table 4). The L' of T2a, T3b, and T4 are $28.9 + 39.0/-12.5$, $14.5 + 5.0/-3.0$, and $19.1 + 21.6/-7.8$ km, respectively, and are close to the eastern geomorphic end point of the fold (about 23 km from the section B-B′ or A-A′ in Figure 3c). The l' of T2a and T3b and of T3b and T4 are $-14.0 + 13.6/-39.0$ and $4.4 + 19.9/-7.1$ km, respectively. In comparison with our geometric models (Figures 14 and 15), we conclude that eastward lengthening of the Mushi anticline ceased by at least ~134 ka (the time of T4 abandonment) and fold growth has been dominated by lateral rotation since then.

7.3. Applications and Limitations of the Model

[38] Our study of the Mushi anticline suggests that, when shortening and uplift rates are well constrained, the lateral growth direction and rates can reliably determined from

Table 4. Associated Parameters Used in Equations (7) and (8) to Constrain Lateral Growth Mechanisms of the Mushi Anticline

Terrace	u_j (m)	$\Delta\varphi_j$	L_j' (km)	l_j' (km)	OSL Age (ka)
T2a	$47.5 + 11.9/-8.6$[a]	$-0.10° \pm 0.03°$	$28.9 + 39.0/-12.5$	-	15.7 ± 2.4
T3b	$137.6 + 57.8/-36.9$	$-0.54° \pm 0.02°$	$14.5 + 5.0/-3.0$	$-14.0 + 13.6/-39.0$	54.7 ± 10.7
T4	$298.5 + 325.1/-120.3$[b]	$-0.89° \pm 0.05°$	$19.1 + 21.6/-7.8$	$4.4 + 19.9/-7.1$	133.9 ± 21.7

[a]The average value of three incremental uplifts since the T2a abandonment in Table 3.
[b]The incremental uplift from the uplift rate multiplied by the OSL age of the T4.

terrace deformation along the fold axis. This method has two obvious benefits. First, terrace geometries allow ready identification of lateral growth mechanisms, especially with respect to the role of rotational steepening of fold tips versus their lateral lengthening. Second, because fluvial terraces are commonly incised into growing folds and their ages can be defined, rates of deformation can be well quantified. In contrast, the dating of successively abandoned wind gaps [*Jackson et al.*, 1996; *Keller et al.*, 1998, 1999] to constrain fold growth rates is commonly difficult and impractical.

[39] This approach, however, has some inherent limitations. First, this model assumes that the geometric pattern of fold growth remains steady through time. If some barrier impedes tip migration, this restriction is assumed to be permanent (within the interval of fold growth being examined). Whereas some fold shapes are consistent with either unrestricted lateral propagation or with long-lasting barriers, the shapes of many folds suggest that barriers restricting tip migration are eventually broken, e.g., *Manighetti et al.* [2001]. If sufficiently old and young terraces were preserved across the former barrier, then the model described here could be applied to terrace remnants on either side of the barrier to define their growth patterns. Second, the model assumes cumulative and incremental uplift along the fold axis varies linearly from a reference point to the fold's tip. Commonly, little field evidence exists to support this assumption, although some studied folds indicate that displacement may remain roughly linear to the fold's tip for the more recent phases of fold evolution [*Manighetti et al.*, 2001], and the data from Mushi are consistent with this assumption. Third, unquantified uncertainties in determining incremental shortening and uplift and other parameters used in equations (7) and (8) may produce large uncertainties when calculating various intersection points and related distances (L_j', l_j'). Such uncertainties are apparent in our Mushi anticline analysis (Table 4) and can make it difficult to constrain whether or not lateral lengthening has occurred. Although these caveats place strong limitations on the model's application, terrace surfaces still provide the most accessible and unambiguous geomorphic criteria to distinguish whether or not lateral rotation has occurred.

8. Conclusions

[40] The Mushi anticline, located at the eastern part of the Pamir Frontal Thrust, is a ~32 km long by 4–10 km wide ESE-trending asymmetrically plunging fold. The structural geometry, topographic longitudinal profile, and drainage pattern indicate that the fold propagated primarily toward the east. Combined geologic mapping and interpreted seismic reflection profiles from neighboring areas suggest that the Mushi anticline is a fault-tip fold controlled by a detachment surface or a blind ramp, with a total shortening of 740 ± 110 m and total structural uplift of ~1300 m.

[41] The northern part of the anticline is dominated by flights of strath terraces. OSL dating defines the ages of terraces T2a, T3b, and T4 to be 15.7 ± 2.4, 54.7 ± 10.7, and 133.9 ± 21.7 ka, respectively: dates that support the increasing widespread recognition that the river incision and terrace formation commonly coincide with major global climate changes [*Pan et al.*, 2003]. In response to ongoing fold growth, the fluvial terraces are clearly deformed. In the northwest, the terraces are cut by a series of subparallel ESE-trending thrust faults. In the middle and eastern fold segments, the terraces are tilted or back-tilted compared to the modern riverbed. Geologic and geomorphic mapping, along with dGPS survey data, reveal that the terrace surfaces display increased slopes with age, thereby indicating that the anticline grew by progressive rotation of the limbs. We use a pure-shear fault-tip fold method to estimate a uniform shortening rate of $1.5 + 1.3/-0.5$ mm/a and uplift rate of $2.3 + 2.1/-0.8$ mm/a. If both rates were constant throughout the fold's history, the fold began growing ~0.5 Ma. The rotation angles of each terrace in the same bedrock domain lessen toward the east and are interpreted to reflect decreased incremental shortening toward the fold's tip.

[42] Parallel to the anticline's axis, longitudinal profiles of terraces also display age-dependent increases in dip. According to our simple model of lateral growth, the eastward lengthening of the Mushi anticline ceased at least ~134 ka, and subsequent fold growth was dominated by steady rates of rotation with little lengthening.

[43] This study from the Mushi anticline illustrates how fluvial terraces can be used to constrain the geometry and rate of three-dimensional folding. With respect to a fold's growth through time, deformed fluvial terraces not only can define the direction and style of lateral lengthening but can also quantify the magnitude and rate of lateral rotation and discriminate between the relative importance of these deformation mechanisms: a difficult task when relying on most other geomorphic criteria. Our model for defining lateral growth mechanisms and rates, however, is both preliminary and simplistic; its inherent and critical assumptions still await verification, and further improvement should emerge from additional, well-calibrated field studies and analog modeling.

Appendix A: Monte Carlo Simulation

[44] The Monte Carlo simulations follow the approach of *Thompson et al.* [2002] and *Amos et al.* [2007, 2010] to estimate uncertainties of the incremental and rates of shortening and uplift, the distance (L'_j) from a reference point to an intersection point and the distance (l'_j) between two intersection points (Figure A1). In our simulations, the probability
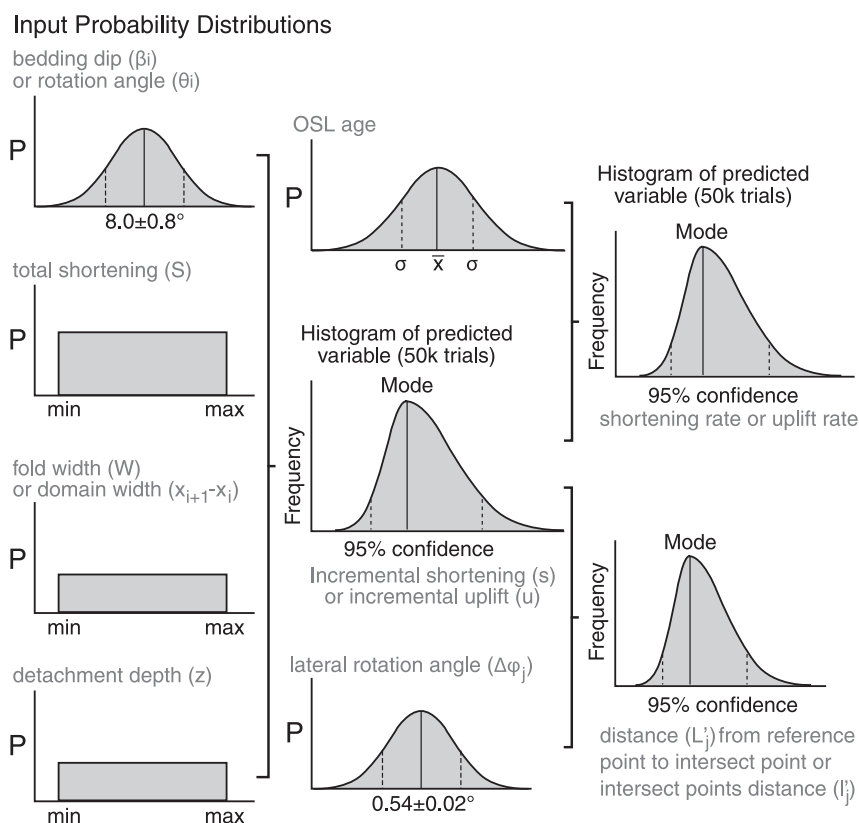
Figure A1. Schematic illustration of the Monte Carlo simulations used to estimate increments and rates of shortening and uplift, distance (L'_j) from the reference point to the intersection point and the distance (l'_j) between two intersection points. This approach draws from a probability distribution of each input parameter to create a histogram of the predicted variable after 50,000 trials. Reported values represent the mode of the output histogram and the associated 95% confidence intervals. Input probability distributions include total shortening (S), detachment depth (z), fold width (W), domain width ($x_{i+1}-x_i$), bedding dip (β_i) of pregrowth strata, rotation angle in cross profile (θ_i), and rotation angle in longitudinal profile ($\Delta\varphi_i$) recorded by terrace surface, as well as the terrace OSL age. Appendix A contains further discussion of these parameters and predicted variables output.

distributions of each input parameter are sampled randomly for 50,000 trials to generate a frequency distribution. Reported values reflect the mode of the output histogram and the associated 95% confidence intervals.

[45] Input parameters take into account total shortening (S), detachment depth (z), fold width (W), domain width ($x_{i+1}-x_i$), bedding dip (β_i) of pregrowth strata, rotation angle in cross profile of terrace surfaces (θ_i), and rotation angle in longitudinal profile of terrace surfaces ($\Delta\varphi_i$) from linear regressions of profile data, as well as the OSL ages of terraces. For tilted terrace surfaces, linear regressions of survey points along cross profiles and longitudinal profiles provide a mean and standard deviation for the rotation angle (θ_i) and the lateral rotation angle ($\Delta\varphi_i$). We assign a ±10% error to the mean of the detachment depth (z), fold width (W), domain width ($x_{i+1}-x_i$), and bedding dip (β_i) of pregrowth strata. We assigned normal distributions to characterize the mean and standard deviation of the rotation angle in cross profile (θ_i), rotation angle in longitudinal profile ($\Delta\varphi_i$), bedding dip (β_i), OSL age, and uniform distributions to characterize the total shortening (S), fold width (W), domain width ($x_{i+1}-x_i$), and detachment depth (z). All simulations output log normal distribution results.

References

Amos, C. B., D. W. Burbank, D. C. Nobes, and S. Read (2007), Geomorphic constraints on listric thrust faulting: Implications for active deformation in the Mackenzie Basin, South Island, New Zealand, *J. Geophys. Res.*, *112*, B03S11, doi:10.1029/2006JB004291.

Amos, C. B., D. W. Burbank, and S. Read (2010), Along-strike growth of the Ostler fault, New Zealand: Consequences for drainage deflection above active thrusts, *Tectonics*, *29*, TC4021, doi:10.1029/2009TC002613.

Bazhenov, M. L., H. Perroud, A. Chauvin, V. S. Burtman, and J.-C. Thomas (1994), Paleomagnetism of Cretaceous red beds from Tadzhikistan and Cenozoic deformation due to India-Eurasia collision, *Earth Planet. Sci. Lett.*, *124*, 1–18, doi:10.1016/0012-821X(94)00072-7.

Benedetti, L., P. Tapponnier, G. C. P. King, B. Meyer, and I. Manighetti (2000), Growth folding and active thrusting in the Montello region, Veneto, northern Italy, *J. Geophys. Res.*, *105*(B1), 739–766.

Bennett, E. R., J. H. Youngson, J. A. Jackson, R. J. Norris, G. M. Raisbeck, F. Yiou, and E. Fielding (2005), Growth of South Rough Ridge, Central Otago, New Zealand: Using in situ cosmogenic isotopes and geomorphology to study an active, blind reverse fault, *J. Geophys. Res.*, *110*, B02404, doi:10.1029/2004JB003184.

Bennett, E., J. Youngson, J. Jackson, R. Norris, G. Raisbeck, and F. Yiou (2006), Combining geomorphic observations with in situ cosmogenic isotope measurements to study anticline growth and fault propagation in Central Otago, New Zealand, *N. Z. J. Geol. Geophys.*, *49*(2), 217–231.

Bernard, S., J. P. Avouac, S. Dominguez, and M. Simoes (2007), Kinematics of fault-related folding derived from a sandbox experiment, *J. Geophys. Res.*, *112*, B03S12, doi:10.1029/2005JB003843.

Bullard, T. F., and W. R. Lettis (1993), Quaternary fold deformation associated with blind thrust faulting, Los Angeles Basin, California, *J. Geophys. Res.*, *98*(B5), 8349–8369.

Burbank, D. W., and R. S. Anderson (2011), *Tectonic Geomorphology*, pp. 310–11, Wiley-Blackwell, Oxford, U. K.

Burbank, D. W., J. K. McLean, M. E. Bullen, K. Y. Abdrakhmatov, and M. M. Miller (1999), Partitioning of intermountain basins by thrust-related folding, Tianshan, Kyrgyzstan, *Basin Res.*, *11*(1), 75–92, doi:10.1046/j.1365-2117.1999.00086x.

Burtman, V. S., and P. Molnar (1993), Geological and geophysical evidence for deep subduction of continental crust beneath the Pamir, Spec. Pap. Geol. Soc. Am., 281, 76 pp.

Charreau, J., C. Gumiaux, J.-P. Avouac, R. Augier, Y. Chen, L. Barrier, S. Gilder, S. Dominguez, N. Charles, and Q. C. Wang (2009), The Neogene Xiyu Formation, a dischronous prograding gravel wedge at front of the Tianshan: Climatic and tectonic implications, *Earth Planet. Sci. Lett.*, *287*, 298–310, doi:10.1016/j.epsl.2009.07.035.

Chen, J., G. S. Qu, J. Hu, and X. Y. Feng (1997), Arcuate thrust tectonics and its contemporary seismicity in the eastern section of the external zone of the Pamir [in Chinese], *Seismol. Geol.*, *19*, 301–312.

Chen, J., D. W. Burbank, K. M. Scharer, E. Sobel, J. Yin, C. Rubin, and R. Zhao (2002), Magnetochronology of the Upper Cenozoic strata in the Southern Chinese Tian Shan: Rates of Pleistocene folding and thrusting, *Earth Planet. Sci. Lett.*, *195*, 113–130.

Chen, J., K. M. Scharer, D. W. Burbank, R. Heermance, and C. S. Wang (2005), Quaternary detachment folding of the Mingyaole anticline, southern Tian Shan [in Chinese], *Seismol. Geol.*, *27*, 530–547.

Chen, J., R. Heermance, D. W. Burbank, K. M. Scharer, J. Miao, and C. S. Wang (2007), Quantification of growth and lateral propagation of the Kashi anticline, southwest Chinese Tianshan, *J. Geophys. Res.*, *112*, B03S16, doi:10.1029/2006JB004345.

Chen, H. L., F. F. Zhang, X. G. Cheng, L. Liao, J. C. Luo, J. Shi, B. Q. Wang, C. F. Yang, and L. F. Chen (2010), The deformation features and basin-range coupling structure in the northeastern Pamir tectonic belt [in Chinese], *Chin. J. Geol.*, *45*, 102–112.

Cowgill, E. (2010), Cenozoic right-slip faulting along the eastern margin of the Pamir salient, northwestern China, *Geol. Soc. Am. Bull.*, *122*, 145–161, doi:10.1130/B26520.1.

Daëron, M., J. P. Avouac, and J. Charreau (2007), Modeling the shortening history of a fault tip fold using structural and geomorphic records of deformation, *J. Geophys. Res.*, B03S13, *112*, doi:10.1029/2006JB004460.

Delcaillau, B., B. Deffontaines, and L. Floissac (1998), Morphotectonic evidence from lateral propagation of an active frontal fold: Pakuashan anticline, foothills of Taiwan, *Geomorphology*, *24*(4), 263–290, doi:10.1016/S0169-555X(98)00020-8.

Epard, J. L., and R. H. Groshong (1993), Excess area and depth to detachment, *AAPG Bull.*, *77*(8), 1291–1302.

Feng, X. Y. (1994), Surface rupture associated with the 1985 Wuqia earthquake, in *Xinjiang [in Chinese], Research on Active Fault (3)*, pp. 45–55, Seismological Press, Beijing.

Goode, J. K., and D. W. Burbank (2011), The temporal evolution of minor channels on growing folds and its bearing on fold kinematics, *J. Geophys. Res.*, *116*, B04407, doi:10.1029/2010JB007617.

Graveleau, F., and S. Dominguez (2008), Analogue modelling of the interactions between tectonics, erosion and sedimentation in foreland thrust belts, *C. R. Geosci.*, *340*, 324–333, doi:10.1016/j.crte.2008.01.005.

Graveleau, F., M. Jacques, and S. Dominguez (2012), Experimental modelling of orogenic wedges: A review, *Tectonophysics*, *538-540*, 1–66, doi:10.1016/j.tecto.2012.01.027.

Hancock, G. S., and R. S. Anderson (2002), Numerical modeling of fluvial strath-terrace formation in response to oscillating climate, *Geol. Soc. Am. Bull.*, *114*, 1131–1142.

Heermance, R. V., J. Chen, D. W. Burbank, and C. S. Wang (2007), Chronology and tectonic controls of Late Tertiary deposition in the southwestern Tian Shan foreland, NW China, *Basin Res.*, *19*, 599–632, doi:10.1111/j.1365-2117.2007.00339.x.

Heermance, R. V., J. Chen, D. W. Burbank, and J. J. Miao (2008), Temporal constraints and pulsed Late Cenozoic deformation during the structural disruption of the active Kashi foreland, northwest China, *Tectonics*, *27*, TC6012, doi:10.1029/2007TC002226.

Hubert-Ferrari, A., J. Suppe, R. Gonzalez-Mieres, and X. Wang (2007), Mechanisms of active folding of the landscape (southern Tian Shan, China), *J. Geophys. Res.*, *112*, B03S09, doi:10.1029/2006JB004362.

Jackson, J., R. Norris, and J. Youngson (1996), The structural evolution of active fault and fold systems in central Otago, New Zealand: Evidence revealed by drainage patterns, *J. Struct. Geol.*, *18*, 217–234.

Keller, E. A., R. L. Zepeda, T. K. Rockwell, T. L. Ku, and W. S. Dinklage (1998), Active tectonics at Wheeler Ridges, southern San Joaquin Valley, California, *Geol. Soc. Am. Bull.*, *110*(3), 298–310, doi:10.1130/0016-7606(1998)110<0298:ATAWRS>2.3.CO;2.

Keller, E. A., L. Gurrola, and T. E. Tierney (1999), Geomorphic criteria to determine direction of lateral propagation of reverse faulting and folding, *Geology*, *27*(6), 515–518, doi:10.1130/0091-7613(1999)027<0515:GCTDDO>2.3.CO;2.

Lavé, J., and J. P. Avouac (2000), Active folding of fluvial terraces across the Siwaliks Hills, Himalayas of central Nepal, *J. Geophys. Res.*, *105*(3), 5735–5770.

Li, T., J. Chen, J. A. Thompson, D. W. Burbank, and W. P. Xiao (2012), Equivalency of geologic and geodetic rates in contractional orogens: New insights from the Pamir Frontal Thrust, *Geophys. Res. Lett.*, *39*, L15305, doi:10.1029/2012GL051782.

Lu, Y. C., X. L. Wang, and A. G. Wintle (2007), A new chronology for dust accumulation in the last 130,000 yr for the Chinese Loess Plateau, *Quat. Res.*, *67*, 152–160.

Manighetti, I., G. C. P. King, Y. Gaudemer, C. Scholz, and C. Doubre (2001), Slip accumulation and lateral propagation of active normal faults in Afar, *J. Geophys. Res.*, *106*(B7), 13,667–613,696.

Molnar, P., et al. (1994), Quaternary climate change and the formation of river terraces across growing anticlines on the north flank of the Tien Shan, China, *J. Geol.*, *102*(5), 583–602.

Mueller, K., and P. Talling (1997), Geomorphic evidence for tear faults accommodating lateral propagation of an active fault-bend fold, Wheeler Ridge, California, *J. Struct. Geol.*, *19*, 397–411, doi:10.1016/S0191-8141(96)00089-2.

Negredo, A. M., A. Replumaz, A. Villaseñor, and S. Guillot (2007), Modeling the evolution of continental subduction processes in the Pamir-Hindu Kush region, *Earth Planet. Sci. Lett.*, *259*, 212–225, doi:10.1016/j.epsl.2007.04.043.

Pan, B., D. W. Burbank, Y. Wang, G. Wu, J. Li, and Q. Guan (2003), A 900 k.y. record of strath terrace formation during glacial-interglacial transitions in northwest China, *Geology*, *31*(11), 957–960.

Rockwell, T. K., E. A. Keller, and G. R. Dembrof (1988), Quaternary rate of folding of the Ventura Avenue anticline, western Transverse Ranges, southern California, *Geol. Soc. Am. Bull.*, *100*, 850–858.

Scharer, K. M., D. W. Burbank, J. Chen, R. J. Weldon, C. Rubin, R. Zhao, and J. Shen (2004), Detachment folding in the Southwestern Tian Shan-Tarim foreland, China: Shortening estimates and rates, *J. Struct. Geol.*, *26*, 2119–2137.

Scharer, K. M., D. W. Burbank, J. Chen, and R. J. Weldon II (2006), Kinematic models of fluvial terraces over active detachment fold: Constraints on the growth mechanism of the Kashi-Atushi fold system, Chinese Tian Shan, *Geol. Soc. Am. Bull.*, *118*, 1006–1021, doi:10.1130/B25835.1.

Schlagenhauf, A., I. Manighetti, J. Malavieille, and S. P. Dominguez (2008), Incremental growth of normal faults: Insights from a laser-equipped analog experiment, *Earth Planet. Sci. Lett.*, *273*, 299–311.

Simoes, M., J. P. Avouac, Y. Chen, A. K. Singhvi, C. Wang, M. Jaiswal, Y. Chan, and S. Bernard (2007), Kinematic analysis of the Pakuashan fault tip fold, west central Taiwan: Shortening rate and age of folding inception, *J. Geophys. Res.*, *112*, B03S14, doi:10.1029/2005JB004198.

Simpson, G. (2004), Role of river incision in enhancing deformation, *Geology*, *32*, 341–344, doi:10.1130/G20190.2.

Sobel, E. R., and T. A. Dumitru (1997), Thrusting and exhumation around the margins of the western Tarim basin during the India-Asia collision, *J. Geophys. Res.*, *102*(B3), 5043–5063, doi:10.1029/96JB03267.

Sobel, E. R., J. Chen, and R. V. Heermance (2006), Late Oligocene-Early Miocene initiation of shortening in the southwestern Chinese Tian Shan: Implications for Neogene shortening rate variations, *Earth Planet. Sci. Lett.*, *247*, 70–81, doi:10.1016/j.epsl.2006.03.048.

Sobel, E. R., L. M. Schoenbohm, J. Chen, R. Thiede, D. F. Stockli, M. Sudo, and M. Strecker (2011), Late Miocene-Pliocene deceleration of dextral slip between Pamir and Tarim: Implications for Pamir orogenesis, *Earth Planet. Sci. Lett.*, *304*, 369–378, doi:10.1016/j.epsl.2011.02.012.

Storti, F., and J. Poblet (1997), Growth strata architectures associated to décollement folds and fault-propagation folds; Inferences on fold

kinematics, *Tectonophysics*, *282*(1-4), 353–373, doi:10.1016/S0040-1951 (97)00230-8.

Suppe, J., G. T. Chou, and S. C. Hook (1992), Rates of folding and faulting determined from growth strata, in *Thrust Tectonics*, edited by K. McClay, pp. 105–121, Chapman and Hall, London.

Thompson, S. C., R. J. Weldon, C. M. Rubin, K. Abdrakhmatov, P. Molnar, and G. W. Berger (2002), Late Quaternary slip rates across the central Tien Shan, Kyrgyzstan, central Asia, *J. Geophys. Res.*, *107*(B9), 2203, doi:10.1029/2001JB000596.

Xiao, A. C., C. Z. Jia, S. F. Yang, G. Q. Wei, H. L. Chen, and C. S. Zhang (2000), The kinematics characters of the thrust-fold belts western front regions in southern Tianshan, China, [in Chinese], *Acta Sedimentol. Sin.*, *18*, 439–444.

Yin, A., S. Nie, P. Craig, T. M. Harrison, F. J. Ryerson, X. Qian, and G. Yang (1998), Late Cenozoic tectonic evolution of the southern Chinese Tian Shan, *Tectonics*, *17*(1), 1–27, doi:10.1029/97TC03140.

Zubovich, A. V., et al. (2010), GPS velocity field of the Tien Shan and surrounding regions, *Tectonics*, *29*, TC6014, doi:10.1029/2010TC002772.